# 國 立 交 通 大 學

## 顯示科技研究所

## 碩 士 論 文

**在二氧化矽基板上具有小圖形尺寸的**

**光子晶體奈米結構雷射特性**

**Laser Emissions from Photonic Crystal Nanostructures with Small Footprints on $SiO_2$ Substrate**

研 究 生：蔡為智

指導教授：李柏璁 教授

中 華 民 國 101 年 8 月

# 在二氧化矽基板上具有小圖形尺寸的光子晶體奈米結構雷射特性

# Laser Emissions from Photonic Crystal Nanostructures with Small Footprints on $SiO_2$ Substrate


研 究 生：蔡為智　　Student：Wei-Chih Tsai

指導教授：李柏璁　博士　　Advisor：Dr. Po-Tsung Lee

國 立 交 通 大 學

顯示科技研究所


碩 士 論 文

A Thesis

Submitted to Department of Photonic and Display Institute

College of Electrical Engineering and Computer Science

National Chiao Tung University

In partial Fulfillment of the Requirements

for the Degree of Master

in

Electro-Optical Engineering

September 2012

Hsinchu, Taiwan, Republic of China

中華民國 101 年 8 月

# 在二氧化矽基板上具有小圖形尺寸的光子晶體奈米結構雷射特性

研究生：蔡為智

指導教授：李柏璁 博士

國立交通大學顯示科技研究所

摘　　要

在二氧化矽基板上具有小圖形尺寸的光子晶體雷射不僅具有結構穩定的特性，更適合整合於積體光路中做為光源元件。而透過三五族材料整合於矽基材料上的奈米結構，更被視為矽奈米光學中有效發光元件的解決方案之一。

在本論文中，透過兩種光子晶體加強光－物質交互作用的機制，輔以 DVS-bis-Benzocyclobutene 黏著接合技術，我們在二氧化矽基板上實現具有小圖形尺寸的光子晶體雷射元件。第一種方式是利用晶格對稱點附近具有極小群速度的光子平帶。基於此機制，我們透過二維正方晶格光子晶體中 $M$ 對稱點的平帶來實現在二氧化矽基板上的帶緣雷射，並做為後續的對照組。接著，藉由消除一個方向的光子晶體，我們在二氧化矽基板上進一步地實現一維光子晶體奈米樑帶緣雷射，其展現出來的元件尺寸以及雷射閾值皆比二維正方晶格光子晶體帶緣雷射來的小。第二種方式則是以形成共振腔來加強光－物質交互作用。基於此機制，我們利用封閉一維光子晶體奈米樑的概念來形成一種新穎的一維光子晶體環形共振腔，在實驗上所展現出來的元件圖形尺寸只有 30 $\mu m^2$，且其環形直徑僅有 3.56 μm。而在實驗上最小能夠觀察到雷射行為的環形直徑僅 3 μm。此外，我們進一步地在一維光子晶體環形結構中設計具有模隙侷限效應的奈米共振腔。相較於一維光子晶體環形共振腔，我們從此種雷射元件可取得較小的模態體積以及較低的雷射閾值。除了極小的元件圖形尺寸外，此類環形光子晶體共振腔可透過側向光波導耦合的方式，在整合於積體光路時，在耦合機制上展現絕佳的可變化性。

# Laser Emissions from Photonic Crystal Nanostructures with Small Footprints on $SiO_2$ Substrate

**Student: Wei-Chih Tsai**

**Advisor: Dr. Po-Tsung Lee**

**Display Institute,**
**National Chiao Tung University**

## Abstract

Photonic crystal (*PhC*) lasers with small device footprint on silicon-dioxide ($SiO_2$) substrate not only has mechanically stable property but also is a good candidate for light sources in condensed photonic integrated circuits (*PIC*s). Moreover, *III-V* active materials on silicon-based substrate are regard as a feasible solution of efficient light sources in silicon photonics.

In this thesis, based on two different mechanisms for enhancing light-matter interactions, DVS-bis-Benzocyclobutene adhesive bonding is utilized to realize ultra-compact *PhC* lasers on $SiO_2$. The first method is using the flat photonic bands with very low group velocities near the highly symmetric points of *PhCs*. Via this mechanism, two dimensional (*2D*) square-*PhC* band-edge (*BE*) lasers at *M* symmetric point are demonstrated for reference. Via eliminating the *PhC*s in one dimension, we further demonstrate one-dimensional (*1D*) *PhC* nanobeam (*NB*) *BE* lasers on $SiO_2$ substrate. Such devices not only have smaller device footprints but also lower threshold value than those of *2D*-square *PhC BE* lasers. The second method is forming resonators to enhance light-matter interactions. Via this mechanism, we propose and realize a novel *1D PhC* ring resonator (*PhCRR*) on $SiO_2$, a design formed by encircling *1D PhC NB*. This kind of device also shows small device footprint of 30 $\mu m^2$. The minimum ring diameter for lasing in experiments is 3 μm. Furthermore, we also design a mode-gap confined nanocavity on *1D PhCR*. Smaller mode volume and lower lasing threshold than those of *1D PhCRRs* are obtained. In addition to small device footprints, lasers based on *PhCRs* also show good flexibility for integrating in *PICs* via side-coupled ridge waveguides.

# Acknowledgements

兩年碩士生涯倏忽即逝，在這艱辛的道路上，首先我要感謝我的指導教授 李柏璁博士在研究上給予的指導。此外，老師對排球的熱情也帶給了全實驗室的人。我想這共同的課外活動使得我們實驗室更顯獨特，也更有凝聚力。謝謝老師。

再者我要感謝 盧贊文大學長，學長在實驗上的討論及精闢的見解讓我少走許多冤枉路。同時，在論文的寫作以及投影片的製作上給予的寶貴意見都讓我受益良多。雖然做為學長在此實驗室的閉門弟子，有太多時候沒能符合學長的期望，但學長總是願意花時間指點我，讓我更有效率的做好我的研究。另外要謝謝 林品佐學長不僅願意在研究上提供協助，也願意分享到許多研究以外的知識，讓我的研究所生涯更顯豐富。

同為 Photonic Technology Lab 的一份子，謝謝 哲嶢、宜錩在 *E*-beam 以及 *SEM* 上的幫忙。謝謝 學弟恆沂在實驗後期提供的協助，讓我能無後顧之憂的專注實驗上的量測，以後你可要好好的對待 *ICP*。謝謝 家揚學長、開昊讓我知道許多表面電漿的知識。謝謝太陽能組的各位： 光揚學長、品睿學姐、佳裕學長、權政、佑政在 *SRO* 的題目上所提供的協助，雖然在此題目上沒能有太大的進展，但是各位在機台以及量測上所提供的協助，都讓我壓力減輕不少。謝謝已經畢業的學長姐們： 邱立勛、林雋威、呂紹平、許書維、莊文齡在我剛進實驗室時，帶領我熟悉實驗室，熟悉新竹的環境。

特別感謝 交通大學 陳方中實驗室以及 中央大學 許晉瑋實驗室在實驗器材以及材料上提供的協助，讓此研究得以順利進行。感謝 交通大學電子所的 張家豪學長在 *ICP* 機台管理上的指導。如果沒有學長的指導，我未必能夠順利解決每一次的 alarm。

感謝 中央大學 陳志強教授在我大學時教過我的任何知識。謝謝大學同學 許鈞筌、陳立人、陳韋先、黃雨平還有高中同學 張博超、張晏豪、陳文傑、陳千越、李佑軒、范國強，雖然你們都很白目，但在我情緒低落、需要人傾聽時你們絕對是很好的朋友。謝謝我從小的好朋友 夏佑賢總是告訴我許多有趣的事情，希望未來你的學生生涯能夠順利。

謝謝我最親愛的家人，總在我需要你們的時候能夠提供慰藉，讓我不致崩潰。

最後，謹以此論文獻給愛我但沒能看到我畢業的外婆及姑姑。

蔡為智 2012 年 9 月 謹誌於 新竹交通大學 交映樓

# Table of Contents

# Table Captions

**Chapter 2**



**Chapter 3**



# Figures Captions

**Chapter 1**



**Chapter 2**

**Chapter 3**

**Chapter 4**

**Appendix A**

# Chapter 1

# Introduction

## 1.1 Photonic Crystal Lasers

Electron manipulation can be achieved in electronic devices by means of electronic band structure in semiconductor materials. This electronic band structure is origin from the superposition of periodic atomic potentials. Similar to electronic band, photonic band can also be induced in a structure named as photonic crystal (*PhC*) with periodic refractive index arrangement. In 1987, two milestone ideas of *PhCs* were proposed by E. Yablonovitch [1] and S. John [2] for spontaneous emission inhibition and photon restriction. Controllable photonic band diagram and photonic band gap (*PBG*) are the fascinating properties of *PhCs*, which realize the manipulation of photons in wavelength scale. According to periodic dimensions, *PhC*s can be classified into one- (*1D*), two- (*2D*) and three-dimensional (*3D*) *PhC*s, as shown in Fig. 1-1. Among these *PhC*s, *2D PhC*s have been widely realized on a suspended slab with finite thickness, as shown in Fig. 1-2, owing to the easiness and feasibility in fabrication. In this structure, with total internal reflection (*TIR*) confinement in vertical direction, the photon manipulations by *PhC*s are available in in-plane directions. Via photonic band engineering or precisely-designed defects, controlling photons in wavelength scale realizes *2D PhC* slab

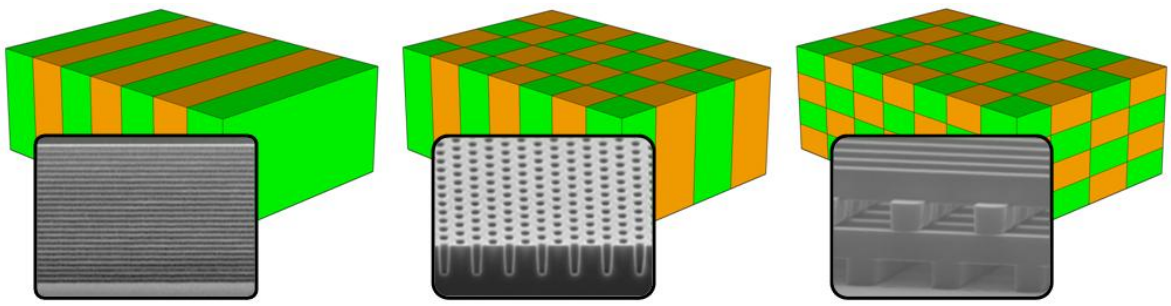

Fig. 1-1: Schemes of *1D*, *2D*, and *3D PhC*s and the corresponding pictures.

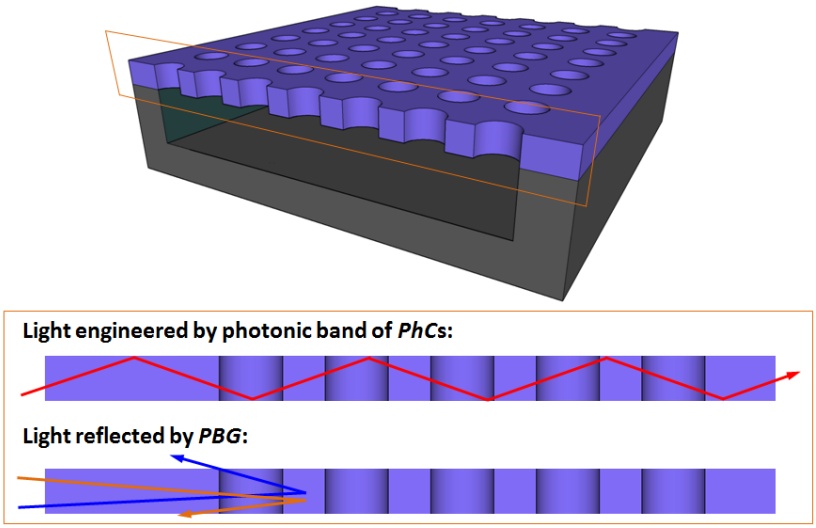


Fig. 1-2: Scheme of photon manipulations in a *2D PhC* slab.

devices with various functions in recent years, for example, optical filters [3,4], optical memory and logic devices [5,6], light emitter sources, and so on [7-9].

Among these applications, *PhC* laser shows excellent properties as a light source in photonic integrate circuits (*PICs*). Generally, there are two main approaches in different *PhC* structures for lasing. The first one is designing a defect in *2D PhCs* to form a resonator via *PBG* effect [10], for example, a *2D PhC* single-defect nanocavity shown in Fig. 1-3(a). The defect can be the size, position, or dielectric constant mismatch of one to several cells in

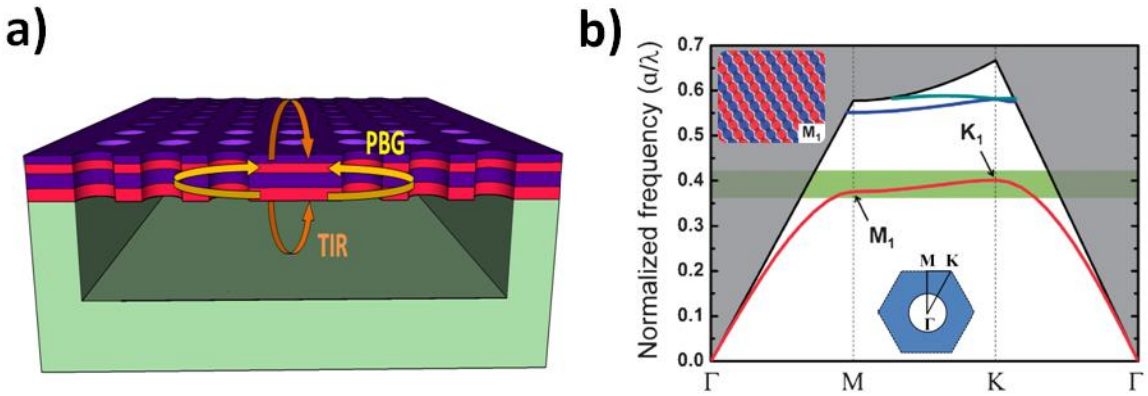


Fig. 1-3: (a) Scheme of a *2D PhC* single-defect nanocavity and its confinement mechanism. (b) Band diagram and *BE* mode profile in magnetic field at $M_1$ point in *2D* hexagonal-*PhC* slab.

*PhCs*. Then the photons will be confined and recycle inside the defect, thus enhances the light-matter interaction and reach lasing.

The other approach is enhancing optical gain via the slow light effect and interference between lattices near the edge of the Brillouin zone [11], that is, at high symmetric points, in a defect-free *PhC* slab. At these high symmetric points, the photonic bands become flat, which means the group velocities ($v_g = \delta\omega/\delta k$) approach zero. The nearly zero group velocity leads to increase of the optical path and time of light-matter interaction, which mainly contributes to lasing. These modes operating at the edge of Brillouin zone are called *PhC* band-edge (*BE*) modes. A typical band diagram of *2D* hexagonal-*PhC* slab and the *BE* mode profile in magnetic field at $M_1$ point are shown in Fig. 1-3(b). Moreover, because there is no local and delicate defect design, this type of *PhC* laser can be fabricated via relatively high throughput fabrication process than using electron beam lithography, for example, laser holography [12], nano-imprint [13], nano-sphere lithography [14], and so on.

In recent years, various lasers with excellent properties have been proposed and demonstrated based on *2D PhC* slabs [14-18]. However, while maintaining various excellent optical properties in wavelength scale, *2D PhCs* also lead to too large device footprint for constructing condensed *PIC*s. In 2008, E. Kuramochi *et al.* tried to partially remove the *2D PhC* periods to reduce the device footprint [19]. However, without sacrificing the devices performances, greatly reducing the footprint in *2D PhCs* system is still challenging [20].

## 1.2 Footprint Minimization of *PhC* Lasers

To break through the bottleneck in minimizing device footprint, *1D PhC* nanobeam (*NB*) will be a feasible solution. This structure was firstly proposed by J. S. Foresi *et al.* in 1997 [21], which is consisted of air holes penetrate into silicon (*Si*) waveguide on silicon-dioxide *($SiO_2$)* substrate, as shown in Fig. 1-4(a) and (b). The photon is confined inside a single defect by *PBG* effect along the waveguide and by *TIR* effect in the other directions. However, the

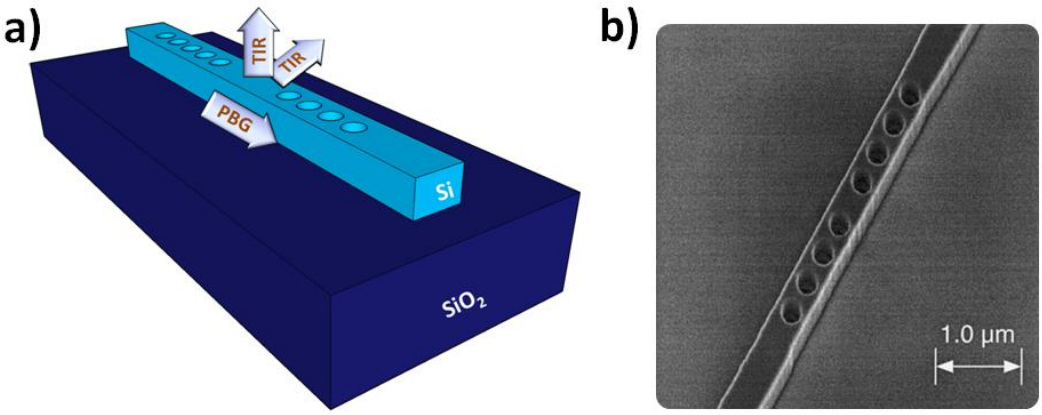


Fig. 1-4: (a) Optical confinement mechanism and (b) *SEM* picture of *1D PhC Si NB* on $SiO_2$ substrate [21].

designed cavity was still lossy on that time. Fortunately, owing to the mature of low-loss nanocavity design principle [22], very recently, versatile *1D PhC NB* devices have been proposed and demonstrated with very small device footprints, including laser light sources [23-26], optical sensing [27], optical manipulation [28], optomechanics [29], and so on.

As the laser light sources, up to date, most demonstrations are based on slab structures. For example, B. H. Ahn *et al.* have demonstrated *1D PhC NB* lasers via mode gap

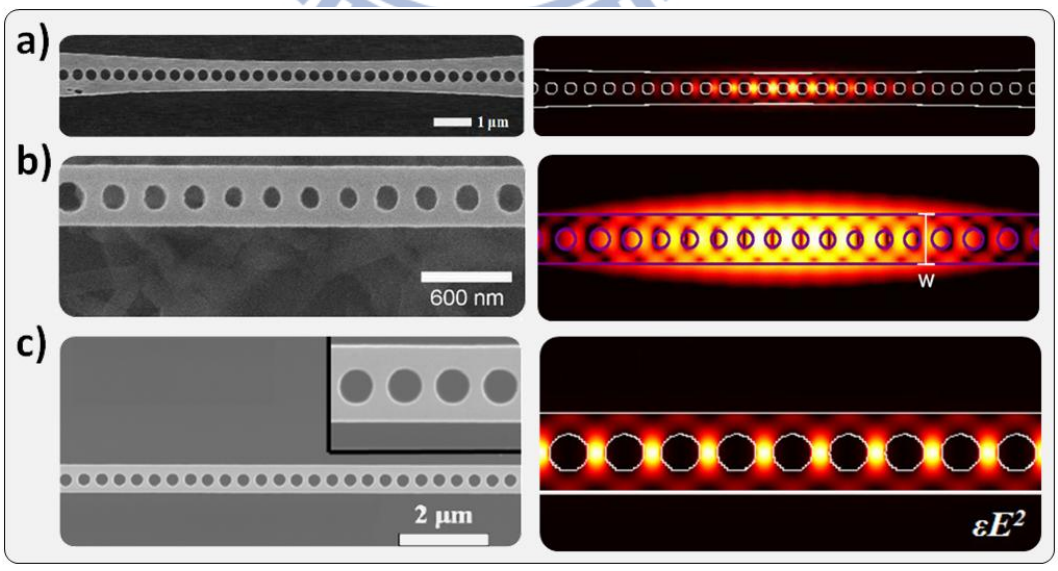


Fig. 1-5: *SEM* pictures and mode profiles of *1D PhC NB* nanocavities with (a) parabolic beam width modulation [23] and (b) effective index matching [24]. (c) *1D PhC NB BE* laser [26].

confinement with parabolic beam width modulation [23], as shown in Fig. 1-5(a). Y. Gong *et al.* [24] and Y. Zhang *et al.* [25] have demonstrated *1D PhC NB* lasers via continuous effective index modulation, as shown in Fig. 1-5(b). In addition, very recently, the *1D PhC NB BE* laser [26] is also reported by Prof. Y. H. Lee in *KAIST*, Korea, as shown in Fig. 1-5(c). Although the slab structure provides good optical confinements, the single-log bridge-like structure also shows mechanical instability and may result in structural collapse [30].

## 1.3 Compact *PhC* Lasers on Asymmetric Structure

To provide mechanically stable supporting for the fragile *1D PhC NB* structures without resulting in huge optical loss, a low refractive index substrate inducing beneath the *PhC NB* can meet the requirements simultaneously. And $SiO_2$ material will be a good candidate not only because of its low index (~ 1.44), but also owing to its good thermal conductivity and low cost.

There have been several widely-used approaches for integrating *III-V* active material onto *Si*-based substrates. The first one is flip-chip integration, which is the most matured technique [31]. In this package level technique, the completed components are flipped and bonded onto *Si*-based substrate. The disadvantage is time consuming due to the alignment issue. The second one is epitaxial growth of *III-V* material on *Si*-based substrates. However, the lattice mismatch between *III-V* material and *Si* results in high density of defects, and degrades the performance of the devices [32]. The third one is bonding technique. This technique not only provides high quality bonding interface, but also allows the following devices fabrication process, which can avoid alignment issue. Recently, various bonding strategies have been demonstrated, including $SiO_2$-$SiO_2$ direct bonding [33], Au/In eutectic bonding [34], spin-on-glass [35], and DVS-bis-Benzocyclobutene (*BCB*) bonding [36-39]. Among these approaches, *BCB* bonding technique shows high reliability and convenience in

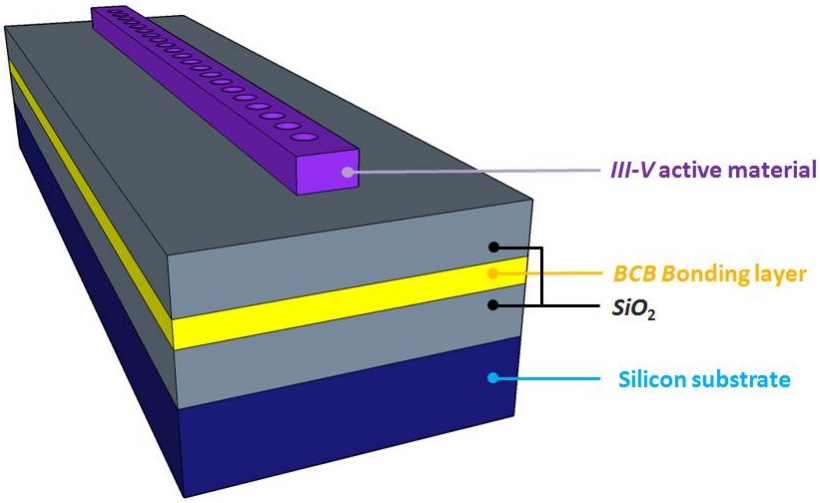


Fig. 1-6: Schematic of *1D PhC NB* (*III-V* material) on low index $SiO_2$ substrate via *BCB* bonding technique.

fabrication process. Therefore, *BCB* bonding technique is used for realizing the *PhC* active (*III-V* material) laser devices with underlying low index $SiO_2$ substrate in this thesis. Scheme of *1D PhC NB* with underlying low index $SiO_2$ via bonding technique is shown in Fig. 1-6.

## 1.4 Motivation and Proposed Structures

To summarize, in this thesis, we want to design and demonstrate *PhC* lasers with ultrasmall footprint and mechanically stable structure. To reach this goal, bonding techniques for integrating *III-V* materials on *Si*-based substrate is applied to realize the structure of *1D PhC NB* on $SiO_2$ substrate. At first, we demonstrate a *2D* square-*PhC BE* laser on $SiO_2$ for reference. And then the device is transformed into a *1D PhC NB BE* laser via eliminating *PhCs* in one dimension. Although S. Kim *et al.* have proposed *1D PhC BE* laser based on slab structure [26], *1D PhC NB BE* laser on $SiO_2$ has not been demonstrated yet.

Based on *1D PhC NB BE* laser on $SiO_2$, we further encircle the *NB* to form a novel *1D PhC* ring resonator (*PhCRR*s) that only can be realized in structure with underlying substrate, as shown in Fig. 1-7(a). *PhCRR*s have been widely developed in *2D PhC* system and applied in various functional devices for *PICs*, such as efficient lasers [40, 41], add-drop filters [42], logical gates [43], optical buffers [44], and so on. However, comparing with *2D PhCRR*s, *1D*

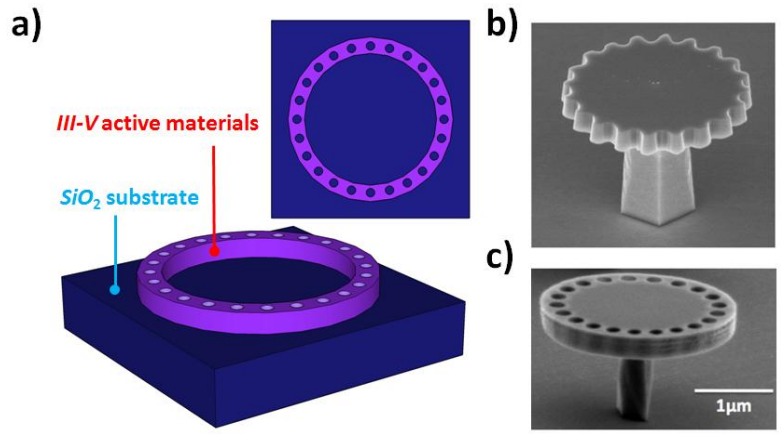


Fig. 1-7: (a) Scheme of *1D PhCRR* formed by an encircled *1D PhC NB* on $SiO_2$. Micro-disks with different circular periodic nanostructure arrangement: (b) grating [45] and air holes [46].

*PhCRR* not only shows much smaller device footprint, but also has higher flexibilities in coupling scheme via side-coupled ridge waveguides in *PIC*s owing to absence of lattice structure restrictions. In addition, unlike the micro-disks with different surrounded periodic designs [45, 46] in Fig. 1-7(b) and(c), only a high *Q* mode can reach lasing in *1D PhCRR*. Based on *1D PhC* ring structure, we also design a mode-gap confined nanocavity for lasers with lower thresholds and smaller mode volumes.

## 1.5 Thesis Overview

The organization of this thesis is illustrated as the following. In chapter 2, fabrication techniques of realizing compact *PhC* lasers on $SiO_2$ will be introduced in details, especially in *BCB* adhesive bonding for integrating *III-V* material on $SiO_2$ substrate. The simulation methods (Plane-wave expansion and finite-element methods) and measurement setup for designing and analyzing the devices will also be introduced. In chapter 3, *2D* square-*PhC* and *1D PhC BE* lasers on $SiO_2$ substrate are demonstrated. The modal properties will be investigated both in simulations and experiments. Then in chapter 4, we will propose, demonstrate and discuss the lasing emission from *1D PhCRR*s and *1D PhC* rings with mode-gap confined nanocavities. Finally, in chapter 5, we will summarize our present and future works.

# Chapter 2

# Simulation Methods, Fabrication Processes, and the Measurement System

## 2.1 Introduction

In this chapter, we will give a briefly introduce to our numerical methods, fabrication processes, and the measurement system for photonic crystal (*PhC*) light emitting devices. In section 2.2, the plane-wave expansion (*PWE*) and the finite-element methods (*FEM*) will be introduced, which can be utilized for calculating band diagram and modal properties of various *PhC* structures. In section 2.3, fabrication processes of forming *PhC* devices on silicon-dioxide ($SiO_2$) substrate will be illustrated. In section 2.4, we will introduce the near-infrared (*NIR*) micro-photoluminescence (micro-*PL*) system used for measuring the emissions from *PhC* devices.

## 2.2 Numerical Simulation Methods for Photonic Crystal

Light propagation in periodic dielectric medium (*PhCs*) can be illustrated by the four Maxwell equations in *MKS* unit:

$$\nabla \cdot \vec{\boldsymbol{B}}(\vec{\boldsymbol{r}}, \mathrm{t}) = 0 \tag{2-1}$$

$$\nabla \cdot \vec{\boldsymbol{D}}(\vec{\boldsymbol{r}}, \mathrm{t}) = \rho \tag{2-2}$$

$$\nabla \times \vec{\boldsymbol{E}}(\vec{\boldsymbol{r}}, \mathrm{t}) + \frac{\partial \vec{\boldsymbol{B}}(\vec{\boldsymbol{r}}, \mathrm{t})}{\partial \mathrm{t}} = 0 \tag{2-3}$$

$$\nabla \times \vec{\boldsymbol{H}}(\vec{\boldsymbol{r}}, \mathrm{t}) - \frac{\partial \vec{\boldsymbol{D}}(\vec{\boldsymbol{r}}, \mathrm{t})}{\partial \mathrm{t}} = \vec{\boldsymbol{J}}(\vec{\boldsymbol{r}}, \mathrm{t}) \tag{2-4}$$

where the $\vec{\boldsymbol{B}}$, $\vec{\boldsymbol{D}}$, $\vec{\boldsymbol{E}}$, $\vec{\boldsymbol{H}}$, $\rho$, $\vec{\boldsymbol{J}}$ are the magnetic flux density, electric displacement, electric fields, magnetic fields, free charges, and current densities. In addition, there are some restrictions in our dielectric medium. The dielectric material should be: (1) Source free material: $\rho$ and $\vec{\boldsymbol{J}}$ are both set to zero. (2) Isotropic material: the terms of $\vec{\boldsymbol{E}}(\vec{\boldsymbol{r}}, \omega)$ and

$\vec{\boldsymbol{D}}(\vec{\boldsymbol{r}},\omega)$ are related by multiplying the term of $\varepsilon_0\varepsilon(\vec{\boldsymbol{r}},\omega)$, where $\varepsilon_0$, $\varepsilon(\vec{\boldsymbol{r}},\omega)$ are permittivity in free space and relative permittivity. And the term of $\varepsilon(\vec{\boldsymbol{r}},\omega)$ is a spatial periodic dielectric function and determined by the different *PhC* structures. (3) Transparent material: the term of $\varepsilon(\vec{\boldsymbol{r}})$ can be treated as positive and real. (4) Non-magnetic material: the term of $\vec{\boldsymbol{B}}(\vec{\boldsymbol{r}},\mathrm{t}) = \mu_0\vec{\boldsymbol{H}}(\vec{\boldsymbol{r}},\mathrm{t})$, where $\mu_0$ is permeability in free space. (5) Frequency independent material. With all of these restrictions, the Maxwell equations (2-1) – (2-4) can be simplified and became as following equations:

$$\nabla\cdot\vec{\boldsymbol{H}}(\vec{\boldsymbol{r}},\mathrm{t}) = 0 \tag{2-5}$$

$$\nabla\cdot[\varepsilon(\vec{\boldsymbol{r}})\vec{\boldsymbol{E}}(\vec{\boldsymbol{r}},\mathrm{t})] = 0 \tag{2-6}$$

$$\nabla\times\vec{\boldsymbol{E}}(\vec{\boldsymbol{r}},\mathrm{t}) + \mu_0\frac{\partial\vec{\boldsymbol{H}}(\vec{\boldsymbol{r}},\mathrm{t})}{\partial\mathrm{t}} = 0 \tag{2-7}$$

$$\nabla\times\vec{\boldsymbol{H}}(\vec{\boldsymbol{r}},\mathrm{t}) - \varepsilon_0\varepsilon(\vec{\boldsymbol{r}})\frac{\partial\vec{\boldsymbol{E}}(\vec{\boldsymbol{r}},\mathrm{t})}{\partial\mathrm{t}} = 0 \tag{2-8}$$

Solutions in electric and magnetic fields are harmonic functions, and can be expressed as the product of spatial and time function separately. The terms of $\vec{\boldsymbol{H}}(\vec{\boldsymbol{r}},t)$ and $\vec{\boldsymbol{E}}(\vec{\boldsymbol{r}},t)$ can be written as the following equations:

$$\vec{\boldsymbol{H}}(\vec{\boldsymbol{r}},t) = \vec{\boldsymbol{H}}(\vec{\boldsymbol{r}})e^{-i\omega t} \tag{2-9}$$

$$\vec{\boldsymbol{E}}(\vec{\boldsymbol{r}},t) = \vec{\boldsymbol{E}}(\vec{\boldsymbol{r}})e^{-i\omega t} \tag{2-10}$$

By substituting equations (2-9) and (2-10), original equations (2-5) – (2-8) will become:

$$\nabla\cdot\vec{\boldsymbol{H}}(\vec{\boldsymbol{r}}) = 0 \tag{2-11}$$

$$\nabla\cdot[\varepsilon(\vec{\boldsymbol{r}})\vec{\boldsymbol{E}}(\vec{\boldsymbol{r}})] = 0 \tag{2-12}$$

$$\nabla\times\vec{\boldsymbol{E}}(\vec{\boldsymbol{r}}) - i\omega\mu_0\vec{\boldsymbol{H}}(\vec{\boldsymbol{r}}) = 0 \tag{2-13}$$

$$\nabla\times\vec{\boldsymbol{H}}(\vec{\boldsymbol{r}}) + i\omega\varepsilon_0\varepsilon(\vec{\boldsymbol{r}})\vec{\boldsymbol{E}}(\vec{\boldsymbol{r}}) = 0 \tag{2-14}$$

The terms of $\vec{\boldsymbol{E}}(\vec{\boldsymbol{r}})$ and $\vec{\boldsymbol{H}}(\vec{\boldsymbol{r}})$ are correlated in equations (2-13) and (2-14). We can get the master equation only relate to $\vec{\boldsymbol{H}}(\vec{\boldsymbol{r}})$ by decoupling these two equations:

$$\nabla \times \left( \frac{1}{\varepsilon(\vec{r})} \nabla \times \vec{H}(\vec{r}) \right) = (\frac{\omega}{c_0})^2 \vec{H}(\vec{r}) \quad (2\text{-}15)$$

where $c_0$ is the vacuum speed of light. Therefore, we can solve (2-15) to find modes $\vec{H}(\vec{r})$ at certain frequency for different *PhC* structures.

In the following sections, we will introduce two numerical simulation methods that for analyzing the *PhC* structures, including plane-wave expansion (*PWE*) and finite-element methods (*FEM*).

### 2.2.1 Plane-Wave-Expansion Method

*PWE* method is an efficiency and useful way to obtain the dispersion relation of a given *PhC* structure. According to the Bloch theorem, eigen-function in a periodic system can be expressed as the product of periodic function and plane-wave envelope function. The main idea of *PWE* simulation is expressing the dielectric function and periodic function in Bloch function as Fourier expansion:

$$\varepsilon^{-1}(\vec{r}) = \sum_{\vec{G}} \varepsilon_{\vec{G}}^{-1} e^{i\vec{G}\cdot\vec{r}} \quad (2\text{-}16)$$

$$\vec{H}(\vec{r}) = \sum_{\vec{G}} \vec{h}_{\vec{k}}(\vec{G}) e^{i(\vec{k}+\vec{G})\vec{r}} \quad (2\text{-}17)$$

where vector $\vec{G}$ is reciprocal lattice vector. The Fourier coefficient, $\varepsilon_{\vec{G}} = \frac{1}{V_c} \int_{unit\ cell} \varepsilon(\vec{r}) e^{-i\vec{G}\cdot\vec{r}}$ and $V_c$ is the volume of the unit cell. By substituting equations (2-16) and (2-17) into master equation (2-15), the master equation becomes:

$$\left(\vec{k}+\vec{G}\right) \sum_{\vec{G}'} \varepsilon_{\vec{G}-\vec{G}'}^{-1} \left(\vec{K}+\vec{G}'\right) h_{\vec{k}}\left(\vec{G}'\right) = -(\frac{\omega^2}{{c_0}^2}) h_{\vec{k}}\left(\vec{G}'\right) \quad (2\text{-}18)$$

With different in-plane *k*-values along the *1st* Brillouin zone, which is determined by the *PhC* structure, several $\vec{G}$ vectors are used to obtain numerous coupled equations. In the computation, proper and finite numbers of plane-waves ($\vec{G}$ vectors) are used to increase

accuracy of the solved dispersion relation. In these coupled equations, we can obtain the eigen-values $(\frac{\omega^2}{{c_0}^2})$ and dispersion relation $(\frac{\omega}{c}\ v.s.\ \boldsymbol{k}_{//})$ by matrix diagonalization method.

### 2.2.2 Finite-Element Method

Finite-element method (*FEM*) is a reliable numerical technique for solving partial differential equations. Therefore, *FEM* is widely used in both physical and engineering area, including heat transfer, fluid mechanics, strain analysis, and electromagnetic. In a standard *FEM* simulation, problems solved by *FEM* should include the following steps [47]:

1. Discretization of the domain of interest: To divide the entire spatial domain *V* into a number of sub-domains, called elements and denoted as $V^e$. ($V^e \equiv$ volume of the element ($e$ = 1, 2, 3…). The number of the elements will greatly affect computation time and accuracy of the results. In our *3D* simulation, tetrahedral elements (shown in Fig. 2-1) are used to construct the geometry of *PhC*s.
2. Selection of an appropriate interpolation function: An interpolation function provides an approximate solution within an element. For simplicity, a linear unknown electric field: $\vec{E}^e(x,y,z) = (a^e + b^e\boldsymbol{x} + c^e\boldsymbol{y} + d^e\boldsymbol{z})$ is used within the element. And the unknown electric field can be expressed as following:

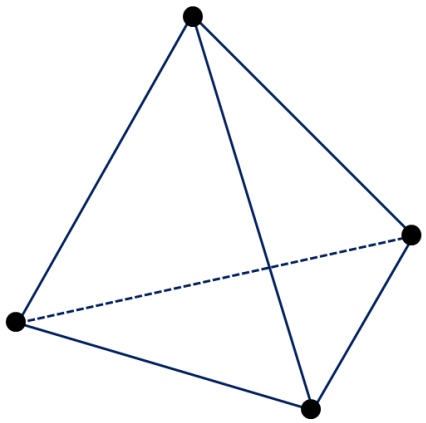

Fig. 2-1: Scheme of the tetrahedral element in *FEM*.

$$\vec{E}^e(x,y,z) = \sum_{j=1}^{4} N_j^e(x,y,z)\,\vec{E}_j^e \tag{2-19}$$

$$[\vec{N}_j^e(x,y,z) = \frac{1}{6V^e}\left(a_j^e + b_j^e x + c_j^e y + d_j^e z\right)]$$

where *j* is the node number in a tetrahedral element.

3. Formulation of the system of equation: Application of the *FEM* to harmonic fields, variational principle can be used to formulate the function and it becomes as:

$$F = \frac{1}{2}\iiint_V \left[\frac{1}{\mu_r}\left(\nabla \times \vec{E}\right)\cdot\left(\nabla \times \vec{E}\right) - {k_0}^2 \varepsilon_r \vec{E}\cdot\vec{E}\right] dV \tag{2-20}$$

where $\mu_r$ and $\varepsilon_r$ are relative permeability and permittivity determined by material.

4. Solution of the system of equations: Substituting equation (2-19) into (2-20), we can obtained:

$$F = \frac{1}{2}\sum_{e=1}^{M}\{\vec{E}^e\}^T[A^e]\{E^e\} - {k_0}^2\{\vec{E}^e\}[B^e]\{E^e\} \tag{2-21}$$

$$[A^e] = \int_{\Omega^e}\frac{1}{\mu_r^e}\left\{\nabla \times \vec{N}^e\right\}\cdot\left\{\nabla \times \vec{N}^e\right\}^T dV,\ [B^e] = \int_{\Omega^e}\varepsilon_r^e\,\vec{E}\cdot\vec{E}\,dV,$$

where $\Omega^e$ and *M* are the computational domain in an element and total number of elements. After carrying out summation, equation (2-21) becomes:

$$F = \frac{1}{2}\left(\{E\}^T[A]\{E\} - {k_0}^2\{E\}^T[B]\{E\}\right) \tag{2-22}$$

with $\delta$F = 0, the eigen-value system is obtained:

$$[A]\{E\} = {k_0}^2[B]\{E\} \tag{2-23}$$

Finally, we can solve equation (2-23) by applying Dirichlet boundary condition.

Once {E} and its eigen-frequency are solved, we can display the electric fields or radiation patterns in the form of slice plots or color pictures. Thus, we use *FEM* to obtain the modal profiles and eigen-frequencies of the desired *PhC* structures.

### 2.2.3 Simulation of Photonic Crystal Device

T o show the reliability of the simulation methods in section 2.2, we calculate the band diagram and modal properties of the dielectric band in a suspended nanobeam (*NB*) with one-dimensional (*1D) PhCs.* Scheme of *1D PhC NB* is shown in Fig. 2-2(a), where *1D PhC*s are composed of the air holes. Several important parameters are also defined in Fig. 2-2(a) including air hole radius *r*, lattice constant *a*, *NB* width *w*, *NB* thickness *t*, and *NB* index $n_{NB}$. With *r/a*, *w*, *t*, and $n_{NB}$ of 0.35, 1.5*a*, 0.8*a*, and 3.4, the same with those in ref. [26], the corresponding band diagram obtained by *3D PWE* method is shown in Fig. 2-2(b).The first three bands are the dielectric, air, and $1^{st}$-order dielectric bands from low to high frequencies. The corresponding mode profiles in $E_y$ fields via *3D FEM* are shown in the inset of Fig. 2-2(b). The results agree quite well with ref. [26].

To investigate a *PhC* structure for laser, knowing it *Q* factor is also necessary. The *Q* factor can be obtained in *FEM* by analyzing the eigen-frequency based on a spring-mass model, which is expressed as:

$$Q = \frac{\omega}{2|\delta|} \tag{2-24}$$

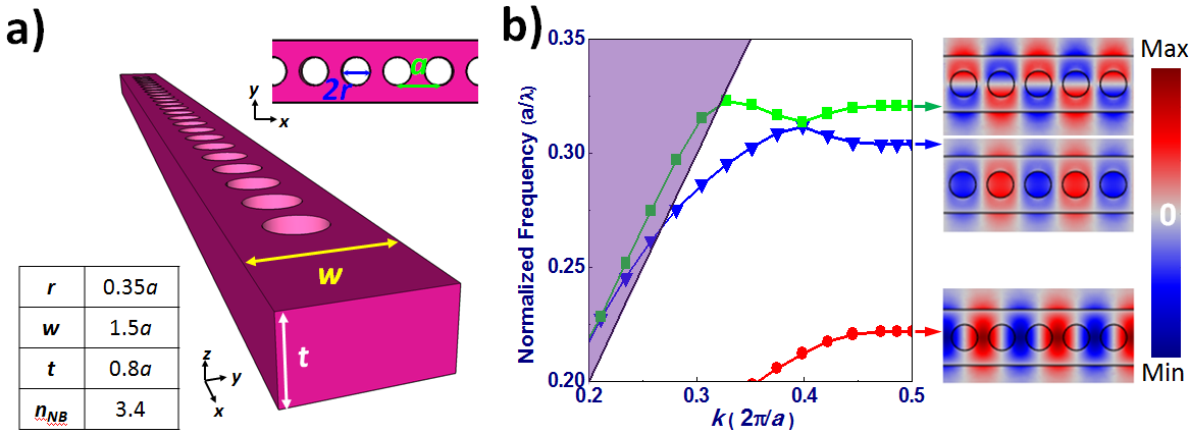


Fig. 2-2: (a) Scheme of *1D PhC NB* and its (b) propagating band diagram via *PWE* method. (c) The mode profiles in $E_y$ field of the first three bands at $k$ = 0.5.

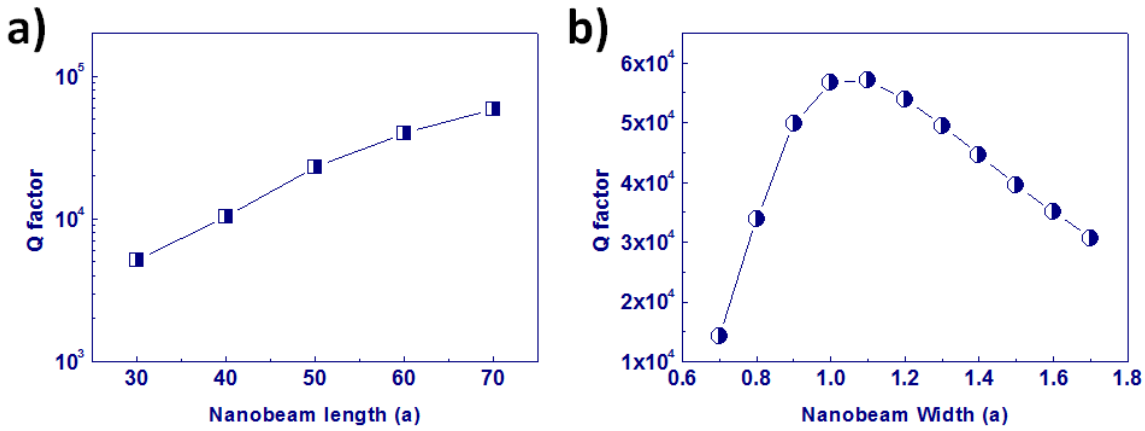


Fig. 2-3: Theoretical *Q* factor of the dielectric bandedge mode as a function of *NB* (a) length and (b) width via *3D FEM*.

where the $\omega$ and $\delta$ are eigen-frequency and damping loss. Via this expression in *FEM*, we calculate the *Q* factor of dielectric band at $k_x$ = 0.5 in *1D PhC NB* with parameters shown in Fig. 2-2(a) and finite *NB* length varied from 30*a* to 70*a*. With fixed *w* of 1.5*a*, the theoretical *Q* factor of the dielectric band at $k_x$ = 0.5 increases monotonically when *PhC* period number increases, as shown in Fig. 2-3(a). In addition, an optimal *Q* value of $5.66\times10^4$ can be obtained when *w* = 1*a* with *NB* length of 60*a*, as shown in Fig. 2-3(b). The results shown in Fig. 2-3(a) and(b) agree quite well with those obtained via finite-difference time-domain (*FDTD*) method in reference [26], which verify the accuracy of the *FEM* simulation for modeling *PhC* nano-structures.

## 2.3 Fabrication Process of *PhC* (*III-V* Materials) Nano-Structue on $SiO_2$

Because of indirect electronic band gap of silicon (*Si*), integration of *III-V* active materials on *Si*-based substrate may be a feasible solution for light emission in *Si* photonics. To reach this goal, various bonding strategies have been demonstrated, including $SiO_2$-$SiO_2$ direct bonding [33], Au/In eutectic bonding [34], spin-on-glass [35], and DVS-bis-Benzocyclobutene (*BCB*) bonding [36-39]. These bonding techniques can realize the *PhC* active optical devices with underlying low index $SiO_2$ on *Si* substrate, which also

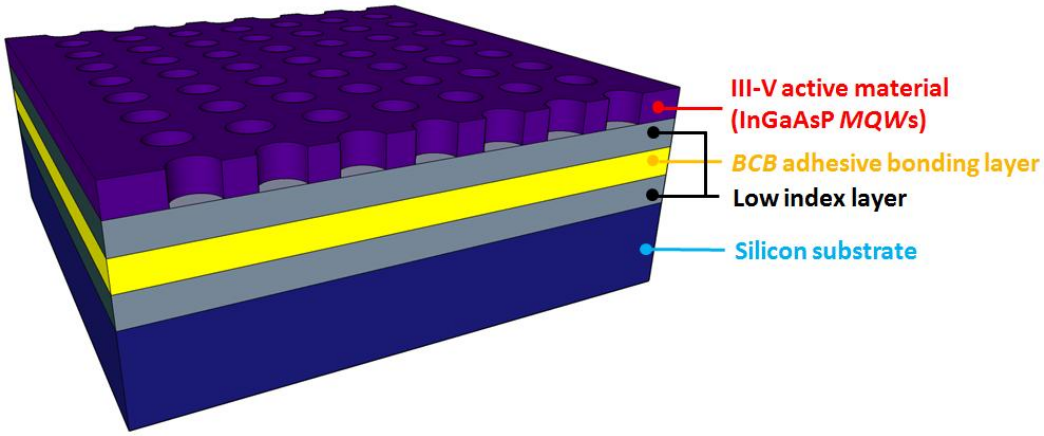


Fig. 2-4: Schematic of *PhC* structure on *III-V* active material (*InGaAsP MQW*s) with underlying low index $SiO_2$ on *Si* substrate.

improve the thermal properties of *PhC* devices. In addition, the asymmetric *PhC* structures also provide stable and reliable mechanical property comparing to the suspended *PhC* slabs. In this thesis, *BCB* adhesive bonding is used to realize the asymmetric *PhC* structure shown in Fig. 2-4. Details of the fabrication processes will be illustrated in the following sections.

### 2.3.1 Transferring *MQWs* on $SiO_2$/*Si* Substrate via Adhesive Bonding

To transfer *III-V* active material onto $SiO_2$ substrate, at first, *InGaAsP MQW*s and *Si* wafers are prepared. The *InGaAsP MQW*s epitaxial structure with *InGaAs* etching stop layer shown in Fig. 2-5(a) is grown by Union Optronics Corp., Taiwan, which has total thickness ranging from 140 to 220 nm and photoluminescence peak near 1550 nm shown in Fig. 2-5(b). Then the *MQW*s and silicon wafer are both deposited by 800 nm $SiO_2$ layer by plasma enhanced chemical vapor deposition (*PECVD*, Oxford Instrument Plasma Technology Plasmalab 80 Plus) shown in Fig. 2-5(c) at 80°C.

To joint these two wafers, adhesive bonding technique via commercial DVS-bis-benzocyclobutene (*BCB*, Cyclotene-4022-35, Dow Chemical Company) is utilized. The steps are illustrated in details in the following and the flow chart is shown in Fig. 2-6.

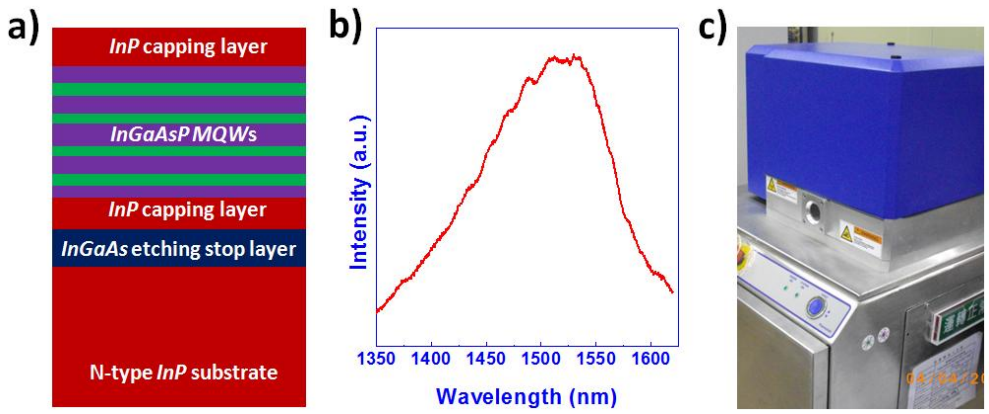


Fig. 2-5: (a) Epitaxial structure of *InGaAsP MQWs* on *InP* substrate and (b) it *PL* spectrum with peak wavelength near 1540 nm. (c) Picture of *PECVD*, facilities of Center for Nano-Science Technology (*CNST*), National Chiao Tung University (*NCTU*).

1. The *BCB* solution is spin-coated on the $SiO_2/Si$ wafer as an adhesive layer and then pre-cured at $60^oC$ for 4 minutes to eliminate the bubbles inside
2. The *InGaAsP MQWs* and $SiO_2/Si$ wafers are clamped together and then hard-baked for *BCB* polymerizing with uniform pressure of 130 *KPa* at $250^oC$ for 2 hours.
3. After the hard-baking process, the *InP* substrate of the *InGaAsP MQWs* is removed via diluted *HCl* (*HCl* : $H_2O$ = 3 : 1) wet-etching at room temperature.
4. Then the *InGaAs* etching-stop and *InP* capping layers are removed via $H_3PO_4$ : $H_2O_2$ : $H_2O$ = 1 : 1 : 8 and *HCl* solutions in sequence to leave *MQWs* on $SiO_2$ substrate.

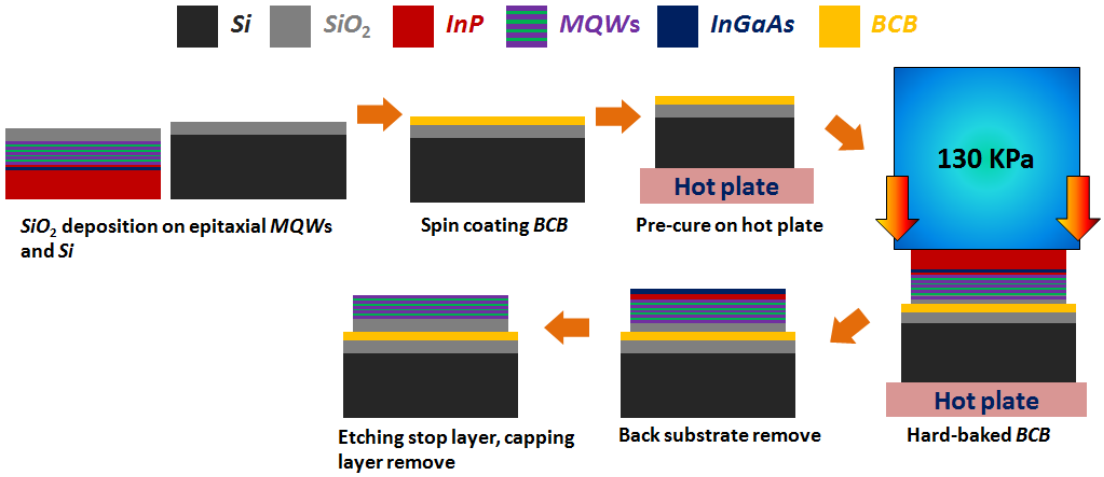


Fig. 2-6: The flow chart of transferring *InGaAsP MQWs* onto $SiO_2$ substrate.

Table 2-1: Average thickness of the *BCB* layer under different spin-coating conditions.

| Condition | Stage 1 | Stage 2 | Avg. *BCB* Layer Thickness |
|---|---|---|---|
| 1 | 1000 *r.p.m*, 10 *sec.* | 4500 *r.p.m*, 30 *sec.* | 6.80 μm |
| 2 | 3000 *r.p.m*, 30 *sec.* | 6000 *r.p.m*, 60 *sec.* | 4.41 μm |
| **3** | **6000 *r.p.m*, 120 *sec.*** | **6000 r.p.m, 120 *sec.*** | **3.54 μm** |

In step 1, the adhesive strength and thickness of *BCB* bonding layer are decided by different spin-coater conditions and diluted ratios. To investigate the properties, at first, the non-diluted *BCB* is spin-coated with different conditions shown in Table 2-1. In Table 2-1, the thickness of *BCB* layer decreases when the spin speed increases. To further reduce the thickness of *BCB* layer, the *BCB* is diluted by mesitylene (*T1100*, Dow Chemical Company) and the diluted ratio is defined as concentration ratio of *T1100*/*BCB*. Condition 3 in Table 2-1 is used to spin-coat the *BCB* with different diluted ratios on $SiO_2/Si$ substrate. In Fig. 2-7(a), the thickness of *BCB* layer decreases when the diluted ratio increases. With *BCB* diluted ratio of 3, the *BCB* bonding layer is as thin as 250 nm. However, too thin *BCB* bonding layer shows

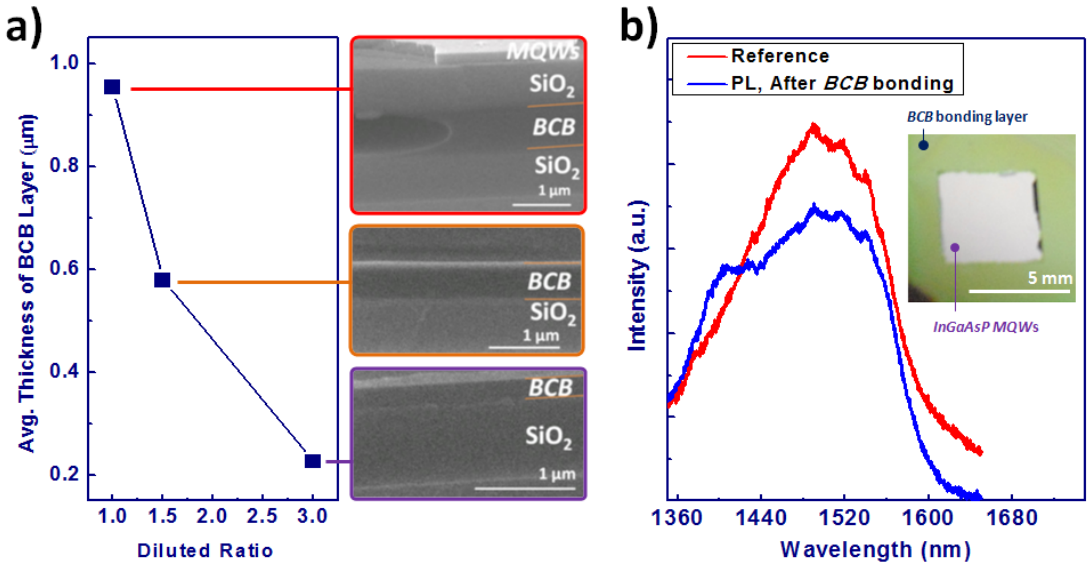


Fig. 2-7: (a) Average thickness of the *BCB* layer under spin coating condition 3 and different diluted ratios shown in Table 2-1. The corresponding cross-section *SEM* pictures are also shown as the insets. (b) *PL* spectrum and picture (inset) of *InGaAsP MQWs* on $SiO_2/Si$ substrate after *BCB* bonding process.

weak adhesive strength between *MQWs* and $SiO_2$. To provide sufficient bonding strength, spin-coater condition 3 and diluted ratio of 1 are used, while the average bonding layer thickness is about 1 μm. The *PL* spectrum and smooth surface of *InGaAsP MQWs* on $SiO_2$/*Si* substrate after *BCB* bonding process are shown in Fig. 2-7(b).

### 2.3.2 Fabrication Processes of Asymmetric *PhC* Device

The *MQWs* on $SiO_2$/*Si* substrate via *BCB* adhesive bonding is then followed by a series of fabrication process illustrated in the following to realize *PhC* nanostructures on it.

1. 70 nm $SiN_x$ hard mask is deposited on the *MQWs* by *PECVD*.
2. 240 nm electron-beam (e-beam) resist is spin-coated on the $SiN_x$ hard mask.
3. *PhC* patterns are defined on *PMMA* by e-beam lithography.
4. Transferring *PhC* patterns from *PMMA* to $SiN_x$ hard mask and from $SiN_x$ to *MQWs* via reactive ion etching (*RIE*) and inductively coupled plasma (*ICP*) dry etching.

Fig. 2-8 shows a flow chart of above fabrication process. The details of each step will be illustrated in the following sections.

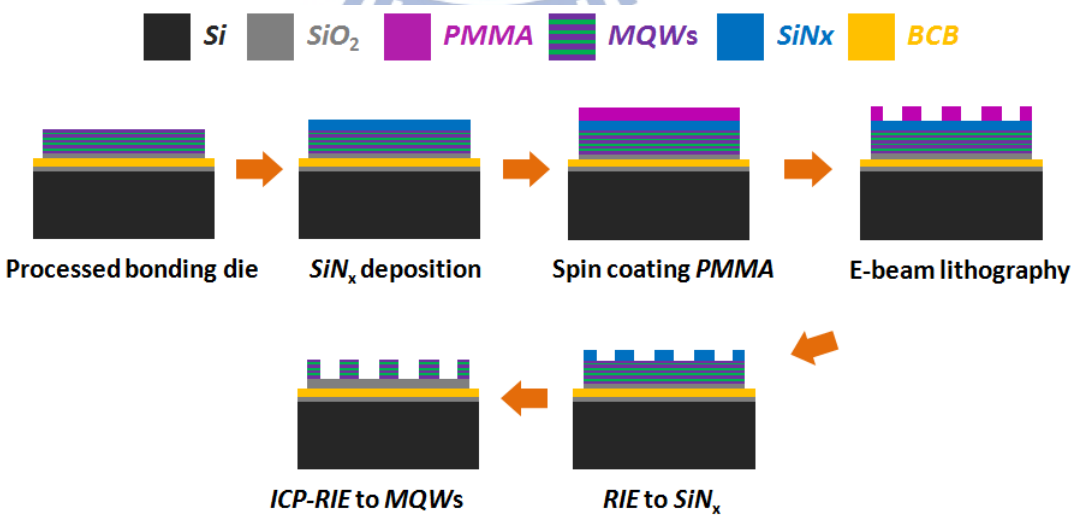


Fig. 2-8: The flow chart of realizing *PhC* structures on the *MQWs* on $SiO_2$/*Si* substrate via *BCB* adhesive bonding.

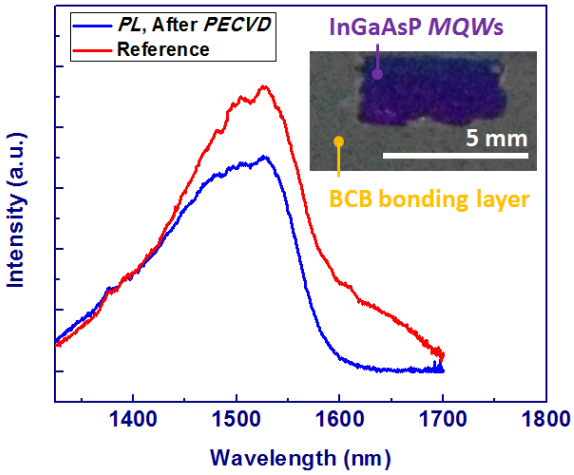


Fig. 2-9: The measured *PL* spectrum and picture (inset) of *MQW*s after depositing $SiN_x$.

### 2.3.3.1 Depositing $SiN_x$ Hard Mask and Defining *PhC* Patterns

First, a $SiN_x$ hard mask with thickness of 70 nm is deposited on the *MQWs* by *PECVD*. The deposition condition is shown in Table 2-2. The picture of *MQW*s after $SiN_x$ deposition and the measured *PL* spectrum are shown in Fig. 2-9. It is worthy to note that the thickness of the $SiN_x$ hard mask is chosen as only sufficient for holding the following *PhC* pattern transferring via *ICP* dry etching. After the *ICP* dry etching, the remaining thickness of the $SiN_x$ hard mask would be less than 10 nm. Thus, the following *RIE* process for cleaning the $SiN_x$ residue, which may etch the underlying $SiO_2$, can be left out. And then we spin-coating 240 nm electron-beam (e-beam) resist (polymethyl methacrylate, *PMMA*) on the deposited $SiN_x$ hard mask. The *PhC* patterns are defined on *PMMA* by e-beam lithography (*EBL*, ELS–7500EX) system shown in Fig. 2-10(a). Finally, the defined *PhC* patterns on *PMMA* are developed by methyl-isobutyl ketone (*MIBK*) and fixed by iso-propyl (*IPA*) solution at 25°C. Fig. 2-10(b) shows the *SEM* picture of *2D PhC*s on *PMMA*.

Table 2-2: $SiN_x$ hard mask deposition condition via *PECVD*.

| $SiH_4$ [sccm] | $NH_3$ [sccm] | $N_2$ [sccm] | T [°C] | P [mTorr] | RF Power [W] | Deposition Rate [nm/min] |
|---|---|---|---|---|---|---|
| 8 | 8 | 250 | 200 | 1000 | 20 | 38.7 |

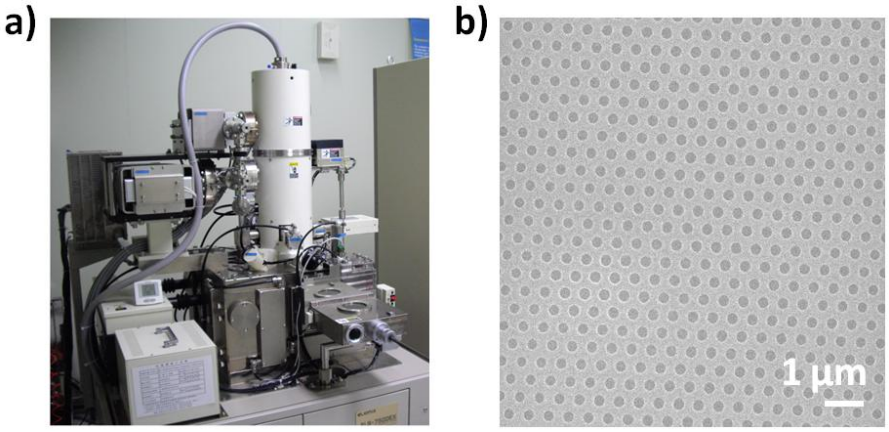


Fig. 2-10: (a) *EBL* system (ELS - 7500EX), facilities of *CNST*, *NCTU*. (b) Top-view *SEM* picture of defined *2D PhC*s on *PMMA*.

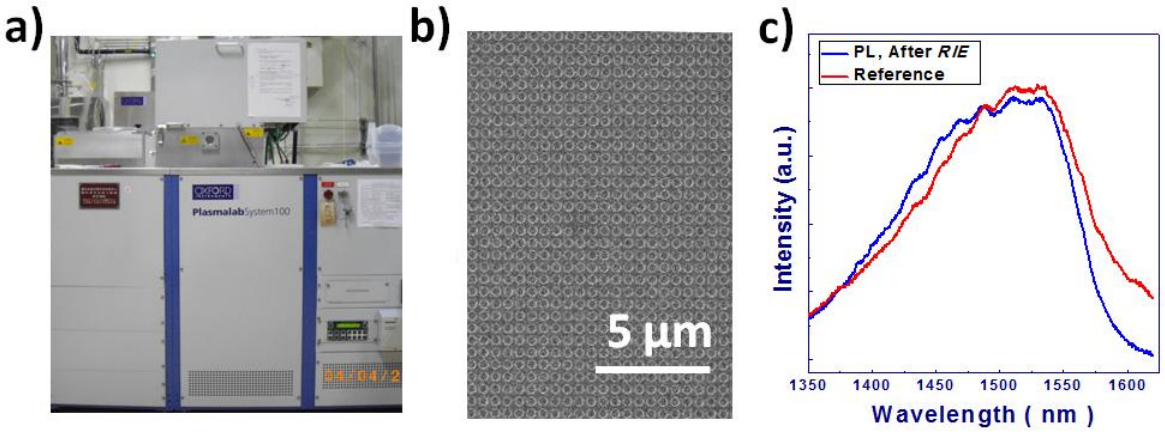


Fig. 2-11: (a) *RIE-ICP* system, facilities of *CNST*, *NCTU*. (b) *SEM* picture of transferred *PhC*s on $SiN_x$ hard mask. (c) The measured *PL* spectrum of *MQW*s after transferring the *PhC* patterns into $SiN_x$ via *RIE*.

### 2.3.3.2 Transferring *PhC* Patterns via Dry Etching Process

To transfer the defined *PhC* patterns on *PMMA* into $SiN_x$ and *MQW*s, the reactive ion etching/inductively coupled plasma (*RIE/ICP*, Oxford Instruments Plasma Technology Plasmalab 100) shown in Fig. 2-11(a) are used. For transferring *PhC* patterns from *PMMA* to $SiN_x$ hard mask, $CHF_3/O_2$ mixed gas in *RIE* etching mode at 20°C is used**.** *SEM* picture of transferred *PhC*s on *SiNx* hard mask is shown in Fig. 2-11(b). The measured *PL* spectrum of *MQW*s after transferring *PhC* pattern into $SiN_x$ via *RIE* in Fig. 2-11(c) only slightly degrades and shows no significant damage on *MQW*s during the *RIE* process.

Then we use $CH_4/Cl_2/H_2$ mixed gas to transfer the *PhC* patterns into *MQWs* in *ICP* etching mode at 20 $^oC$. Dry etching at low temperature can avoid the phase change of *BCB* bonding layer. The etching rate of *InP/InGaAsP* is about 412 nn/min and selectivity ratio to $SiN_x$ is about 5. The recipe of *RIE* and *ICP* etching modes are listed in Table 2-3. The measured *PL* spectrum of *MQW*s after *ICP* dry etching is shown in Fig. 2-12(a). Fig. 2-12(b) shows the top-view *SEM* picture of square-*PhCs* on *InGaAsP MQW*s on $SiO_2/Si$ substrate after a series of dry etching steps. The zoom-in tilted-view *SEM* picture in the inset of Fig. 2-12 shows the etching profile and clearly observed underlying $SiO_2$. Fig. 2-13 shows the overview of fabrication processes of *PhC* light emitters based on *InGaAsP MQW*s on $SiO_2/Si$ substrate.

Table 2-3: Recipe of *RIE* and *ICP* mode.

| | CHF3 [sccm] | $O_2$ [sccm] | $CH_4$ [sccm] | $Cl_2$ [sccm] | $H_2$ [sccm] | T [$^oC$] | P [mTorr] | RF Power [W] | ICP Power [W] |
|---|---|---|---|---|---|---|---|---|---|
| *RIE* Mode | 50 | 5 | - | - | - | 20 | 55 | 150 | - |
| *ICP* Mode | - | - | 4.5 | 8.5 | 3.5 | 20 | 4 | 100 | 1200 |

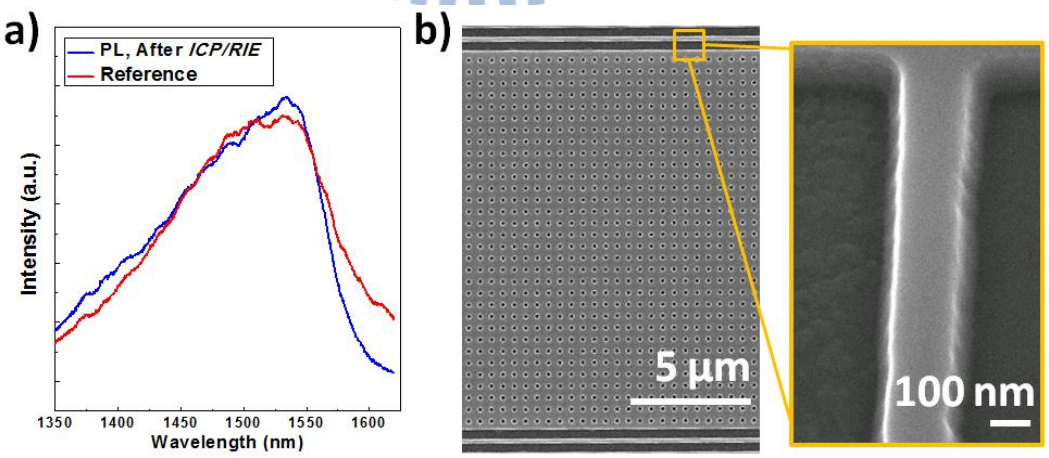


Fig. 2-12: (a) The measured *PL* spectrum of *MQW*s after transferring *PhC* pattern into *MQW*s via *ICP* dry etching. (b) Top- and tilted-view *SEM* pictures of a square-*PhC*s on $SiO_2/Si$ substrate.

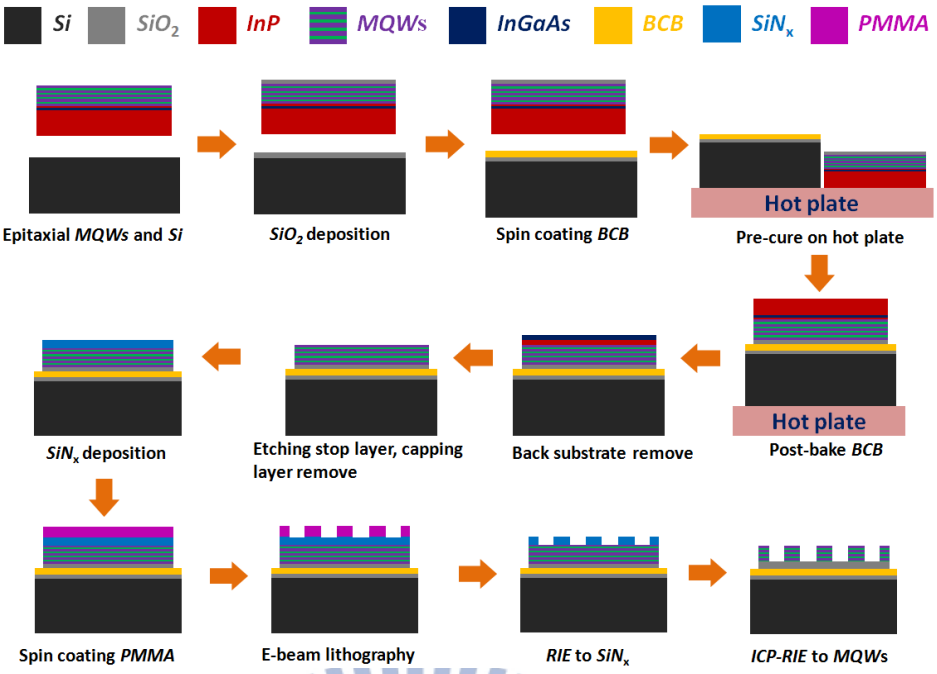


Fig. 2-13: Flow chart of fabricating *PhC* nano-structures on *MQWs* on $SiO_2$/*Si* substrate.

## 2.4 Measurement Setup

Fig. 2-14 shows the scheme of *NIR* confocal micro-*PL* system for characterizing the light emissions from *PhC* nano-structures. In this measurement setup, an 845 nm transistor-transistor logical (*TTL*) laser (Power Technology *Inc.*, APMT-60) with pulse or continuous-wave (*CW*) operations is used for pumping the devices. For the pulse operation, the output current from the *DC* power supply is modulated by a function generator (Stanford *Inc.*, DG-535). An attenuator and a depolarizer are put in front of the laser to control the output power and maintain the un-polarization of the pump laser. The pump laser beam is split into two beams by a 50/50 beam splitter (Thorlabs, BP-150). One beam is focused on the sample with about 6 μm pump spot sizes in diameters on the *PhC* devices by 50x long working distance objective lens (*NA* = 0.42) (Mitsutoyo, M-plan 50x). The other beam is fed into a silicon power meter to estimate the power pump on the sample. The sample is mounted on a 3-axes piezo-stage used to adjust the alignments between the pumping spot and *PhC* devices. A microscopic system with co-axial white light source and a charge-coupled device (*CCD*) is used to monitor this adjustment. The light emission is collected by the 50x long

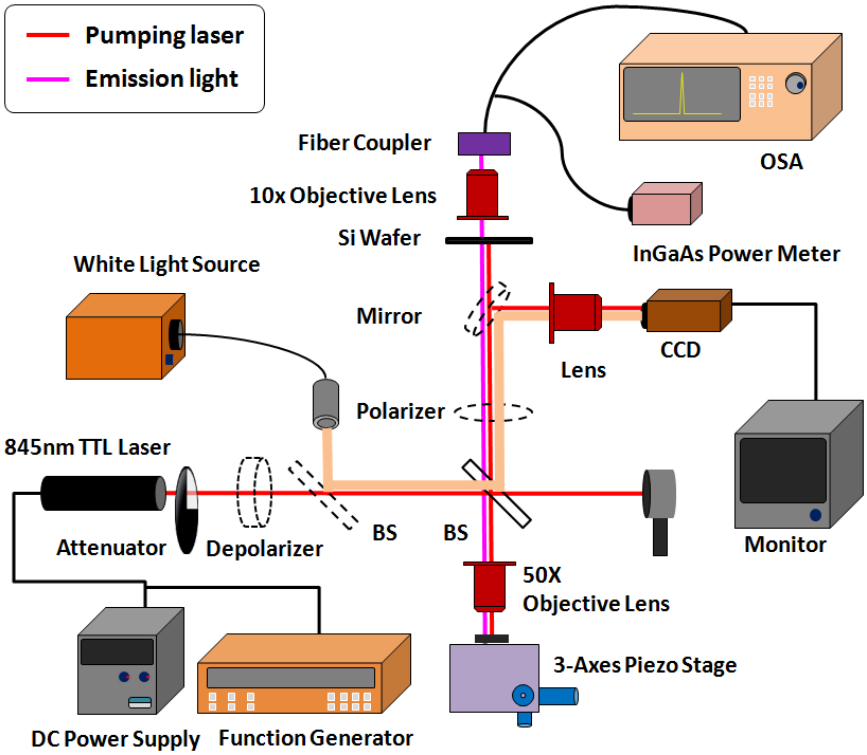


Fig. 2-14: Schematic of the *NIR* confocal micro-*PL* measurement system.

working distance objective lens and fed into a multimode fiber (*MMF*) via a 10x objective lens. To block the reflected pump light, a doubly-polished silicon wafer is put in front of the lens. Then the emission is analyzed by an optical spectrum analyzer (*OSA*) (Ando *Inc*., AQ-6315A) and a *InGaAs* power meter (Advantest *Inc*., Q8221).

## 2.5 Demonstration of Microdisk Laser on $SiO_2/Si$ substrate

To simply confirm the laser emission can be obtained from the resonator based on the *MQW*s on $SiO_2/Si$ substrate, we fabricate a microdisk with diameter of 3.56 μm on $SiO_2/Si$ substrate, as shown in Fig. 2-15(a) and (b). In measurements, under optical pulse excitation with 6.7 mW peak powers, a single mode lasing at 1538.2 nm is observed, as shown in Fig. 2-15(c). The theoretical whispering-gallery (*WG*) mode profile in electric field with azimuthal number of 15 obtained from *3D FEM* simulation is also shown as the inset in Fig. 2-15(c). This demonstration implies that we can demonstrate different kinds of nano-photonic light emitters based on this asymmetric structure.

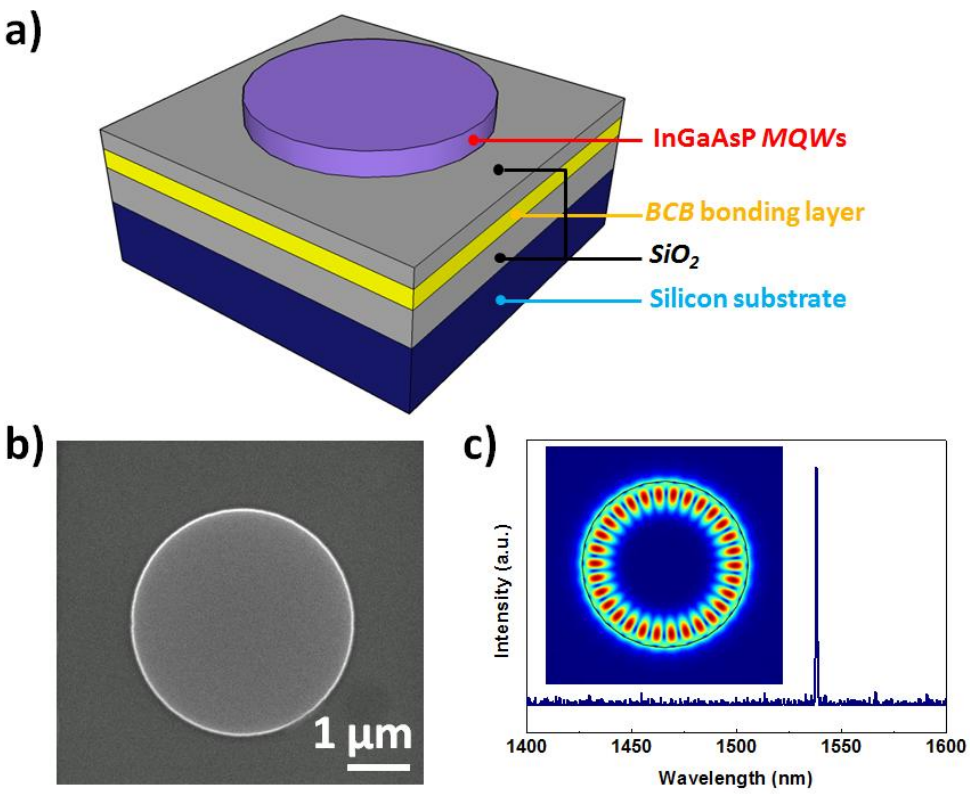


Fig. 2-15: (a) Scheme of a microdisk on *$SiO_2$/Si* substrate. (b) Top-view *SEM* picture and (c) single mode lasing spectrum at 1538.2 nm of a microdisk with 3.56 μm in diameter on *$SiO_2$/Si* substrate. Theoretical lasing *WG* mode profile in electric field with azimuthal number of 15 via *3D FEM* is shown as the inset of (c).

## 2.6 Summary

In this chapter, we have introduced the numerical methods, including *PWE* and *FEM* for modeling *PhC* nanostructures. The modal properties of the dielectric band in *1D PhC NB* are also simulated to guarantee the accuracy of the methods. The *BCB* adhesive bonding techniques and nano-fabrication processes of *PhCs* are also introduced for realizing *PhC* active (*InGaAsP MQWs*) devices on *$SiO_2$/Si* substrate. The *NIR* micro-*PL* system used to characterize the optical properties of fabricated *PhC* devices is also introduced. To verify this asymmetric structure is feasible for active nanophotonic devices, single *WG* mode lasing emission from a microdisk with 3.56 μm in diameter on *$SiO_2$/Si* substrate is demonstrate.

# Chapter 3

# Photonic Crystal Band-Edge Lasers on $SiO_2$ Substrate

## 3.1 Introduction

As we mentioned in chapter 1, photonic crystal (*PhC*) band-edge (*BE*) laser utilizes the flat photonic band with local group velocity $v_g \sim 0$ near high symmetric points to enhance light-matter interactions and achieves lasing operations. Owing to this mechanism, this kind of device shows less requirement of high *Q* design in achieving lasing. In addition, because the *BE* mode lasing occurs in the *PhCs* with large area and without delicate defect design, this type of device can be fabricated by high throughput fabrication processes with large fabrication tolerance. However, this feature also leads to a very large device footprint. In chapter 3.2, at first, we demonstrate and investigate the lasing properties of two-dimensional (*2D*) square-*PhC BE* laser on $SiO_2$ substrate both in simulations and experiments for reference. To further reduce device footprint of the *2D* square-*PhC*, *PhCs* are eliminated in one dimension and lead to a *1D PhC* nanobeam (*NB*) *BE* laser on $SiO_2$ substrate. The modal properties in simulation and lasing characteristics in experiments are shown and discussed in chapter 3.3.

## 3.2 Optical Properties of *2D* Square-*PhC BE* Lasers on $SiO_2$ Substrate

Scheme and top-view scanning electronic microscope (*SEM*) picture of *2D* square *PhC BE* laser on $SiO_2$ substrate are shown in Fig. 3-1(a). To understand the *BE* mode in *2D* square-*PhC* on $SiO_2$, at first, we calculate the transverse-electric (*TE*)-like photonic band diagram of *PhCs* with air-hole radius (*r*) over lattice constant (*a*) (*r/a*) ratio of 0.22 and *InGaAsP* multi-quantum-wells (*MQWs*) thickness *t* of 200 nm by three-dimensional (*3D*) plane-wave expansion (*PWE*) method, as shown in Fig. 3-1(b). The indices of $SiO_2$ ($n_{SiO2}$) and

*InGaAsP* ($n_{InGaAsP}$) are set as 1.44 and 3.4 respectively. In Fig. 3-1(b), we focus on the first two bands from low to high frequencies below light-line (slab modes). Via *3D* finite element method (*FEM*), the *BE* mode profiles in electric fields of the first and second bands at high symmetric *X* and *M* points, denoted as $X_0$, $X_1$, $M_0$, and $M_1$, are show in Fig. 3-1(c).

To evaluate which mode will be the lasing mode in our design, at first, the gain region of *InGaAsP MQW*s (red shadow region in Fig. 3-1(b)) overlaps with the modes are considered. In Fig. 3-1 (b), obviously, $M_0$, and $M_1$ *BE* modes coincide with the gain region. Second, from the mode profiles in electric fields in Fig. 3-1(d), both $M_0$ and $M_1$ *BE* mode shows strong field

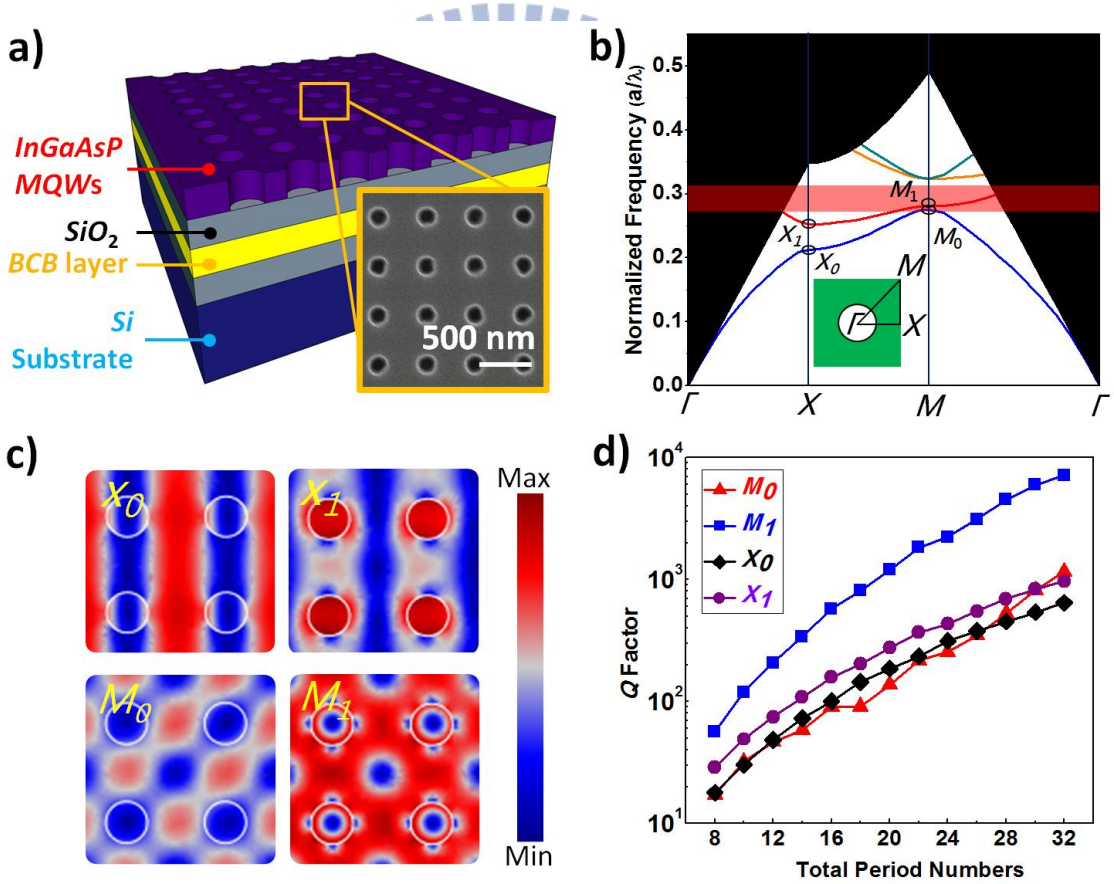


Fig. 3-1: (a) Scheme and top-view *SEM* pictures of *2D* square-*PhCs* on $SiO_2$ substrate. (b) The photonic band diagram of *2D* square-*PhCs* with $r/a$ = 0.22 and $t$ = 200 nm on $SiO_2$ substrate via *3D PWE* method. The gain region of *InGaAsP MQW*s is denoted by the red shadow. (c) Simulated electric field distribution of $X_0$, $X_1$, $M_0$, and $M_1$ *BE* modes by *3D FEM*. (d) Theoretical *Q* factors of $X_0$, $X_1$, $M_0$, and $M_1$ *BE* modes in *2D* square-*PhC* on $SiO_2$ under different total period numbers.

concentrates in the dielectric region, which means stronger light-matter interactions. In addition, quality ($Q$) factor is also the key property for deciding a mode lasing or not. Thus, the $Q$ factors of $X_0$, $X_1$, $M_0$, and $M_1$ *BE* modes under different total period numbers are calculated by *3D FEM* and shown in Fig. 3-1(d). In Fig. 3-1(d), we can see the $Q$ factor of $M_1$ *BE* mode is always higher than the other three modes. Therefore, $M_1$ *BE* mode should be the lasing mode in the device. In our following fabrication, total period numbers of the devices are chosen to be 32, while the $Q$ factor of $M_1$ *BE* mode is ~ $7 \times 10^3$.

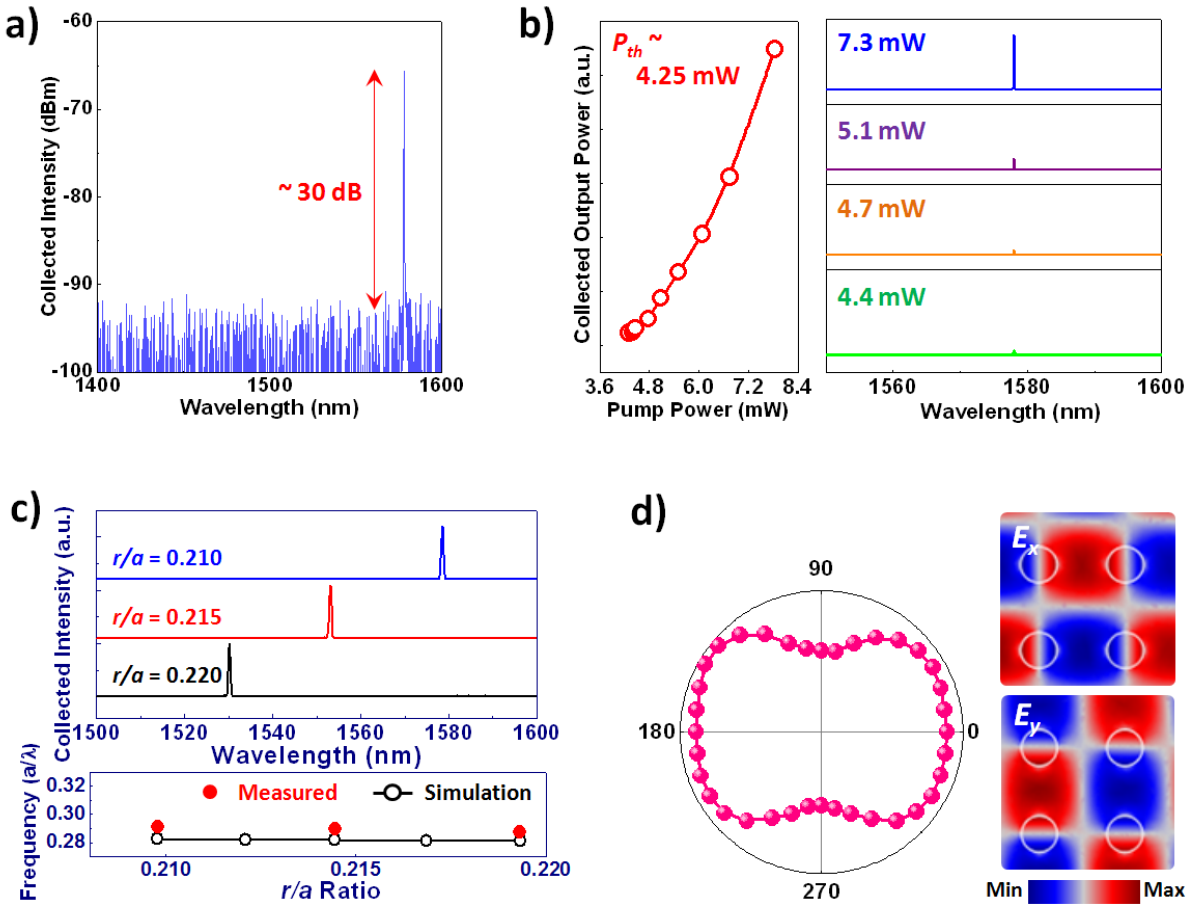


Fig. 3-2: (a) Measured lasing spectrum in *dB* scale with lasing wavelength at 1578 nm and *SMSR* of 30 *dB* from *2D* square-*PhC BE* laser on $SiO_2$. (b) *L-L* curve of *2D* square-*PhC BE* laser on $SiO_2$ shows threshold power of 4.25 mW. The inset shows the lasing spectra under different pump power. (c) Lasing spectra from *2D* square-*PhC* on $SiO_2$ under different *r/a* ratios and the measured lasing frequencies and simulated $M_1$ mode frequency under different *r/a* ratio of *2D* square-*PhC BE* laser on $SiO_2$. (d) The measured polarization with polarized ratio of 1.8. The simulated $E_x$ and $E_y$ fields of $M_1$ *BE* mode is also shown as the insets.

Table 3-1: Duty cycle used in different structures.

| | Duty Cycle |
|---|---|
| *PhC* Lasers on $SiO_2$ Substrate | 1.5 – 2 % |
| *2D PhC* Lasers on Suspended Slab | 0.75 % |
| *1D PhC* Lasers on Suspended *NB* | 0.15 % |

The devices are optically pumped via 845 nm diode laser with 15 ns pulse width. In the following measurements of *PhC* lasers on $SiO_2$ in this thesis, 1.5 - 2 % duty cycle is used, which are higher than the values that we usually used in suspended structures, as shown in Table 3-1. This is attributed to the underlying $SiO_2$ with good thermal conductivity.

The measured single mode lasing spectrum at 1578 nm from a device with $a$ = 460 nm and $r/a$ ratio = 0.21 is shown in Fig. 3-2(a), which shows high side-mode suppuration ratio (*SMSR*) of 30 *dB*. And the measured light-in light-out (*L-L*) curve shows a threshold power of 4.25 mW. This milli-watt level threshold value is owing to the large pump area and the underlying lossy $SiO_2$ layer. Lasing spectra under different pump power from 4.4 to 7.3 mW are also shown as the inset of Fig. 3-2(b). Only single mode lasing is observed, which is the feature of *BE* laser.

To identify this lasing mode, the measured lasing spectra from *2D* square-*PhCs* with different $r/a$ ratios on $SiO_2$ are shown in Fig. 3-2(c), where the lasing wavelength shows a red shift when $r/a$ decreases. In Fig. 3-2(c), the measured wavelengths match with simulated frequencies of $M_1$ *BE* mode under different $r/a$ ratios via *3D PWE* simulation. The difference between simulated results and measured results may come from the fabrication imperfection, thickness variation of *MQW*s, or value estimated from *SEM* picture. Therefore, we can conclude the lasing mode is the $M_1$ *BE* mode. To further confirm this, polarization of the lasing mode is also measured, as shown in Fig. 3-2(e). The low polarized ratio of 1.8 is because neither $E_x$ nor $E_y$ fields dominate in the $M_1$ *BE* mode, as shown in the insets of Fig. 3-2(d).

Although we demonstrate *2D* square-*PhC BE* laser on $SiO_2$ substrate via $M_1$ *BE mode*. High threshold of 4.25 mW is not only attributed to the lossy $SiO_2$ substrate, but also owing to the large device footprint of 14.8 × 14.8 $\mu m^2$ caused by *2D* square-*PhCs*. The definitions of device footprints of *PhC* lasers investigated in this thesis are given in Appendix A. To reduce the device footprint and threshold, eliminating *PhCs* in one-dimension to form *1D PhC NB* investigated in the next section will be a feasible solution.

## 3.3 *1D PhC NB BE* Lasers on $SiO_2$ Substrate

To further reduce the device footprint, we investigate a *1D PhC NB BE* laser on $SiO_2$ substrate, which is formed by periodic air holes on a ridge waveguide on $SiO_2$ substrate, as shown in Fig. 3-3(a). Actually, this structure can be regarded as eliminating *PhCs* in *2D* square-*PhCs* in one dimension. The important parameters are defined in Fig. 3-3(a), including *NB* thickness ($t$), *NB* width ($w$), air-hole radius ($r$), lattice constant ($a$), refractive index of *NB* ($n_{NB}$), and refractive index of $SiO_2$ ($n_{SiO2}$). With $t$ = 200 nm, $w$ = 1.4$a$, and $r/a$ = 0.33, the simulated band diagram of *1D PhC NB* on $SiO_2$ via *3D PWE* method is shown in Fig. 3-3(b). The first three bands from low to high frequencies are dielectric-, air-, and $1^{st}$-order dielectric

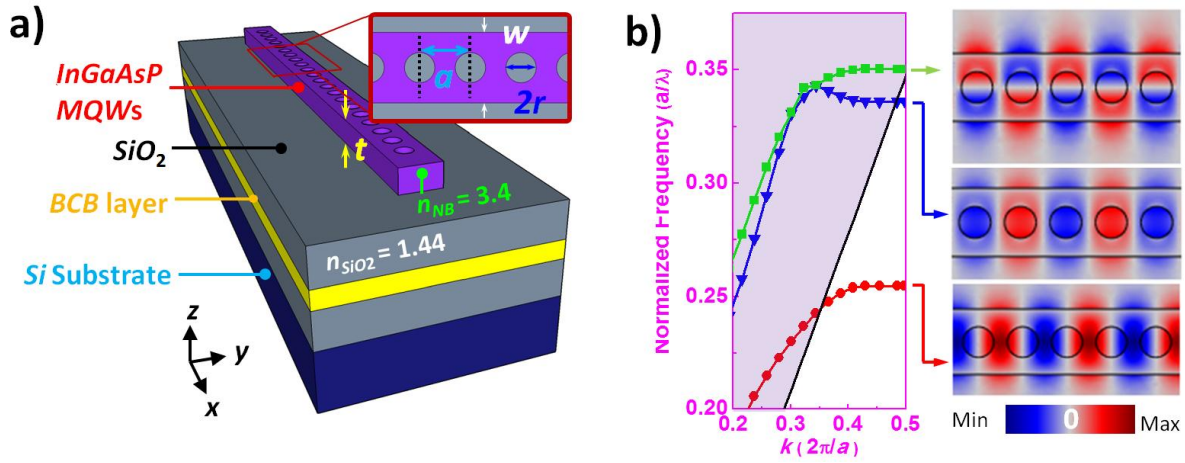


Fig. 3-3: (a) Scheme and important parameters of *1D PhC NB* on $SiO_2$ substrate. (b) Photonic band diagram of *1D PhC NB* on $SiO_2$ substrate via *3D PWE*. The mode profiles in $E_y$ fields of the first three bands at $k_x$ = 0.5 are also shown as the inset.

bands respectively. Their mode profiles in $E_y$ fields at $k$ = 0.5 via *3D FEM* are shown as inset of Fig. 3-3(b). According to their mode profiles, the dielectric band shows good overlaps with the gain medium, which is beneficial for active laser. Therefore, in the following researches, we will focus on the dielectric mode only.

### 3.3.1 Modal Properties of Dielectric Band in Simulations

At first, we calculate the wavelength, *Q*, and *V* of the dielectric mode in *1D PhC NB* on $SiO_2$ as a function of total *PhC* period numbers (*P*), as shown in Fig. 3-4(a) and (b). The effective mode volume *V* is expressed as:

$$V = \frac{\int \varepsilon |E|^2 dV}{\int \varepsilon(r_{max})|E_{max}|^2 dV} \tag{3-1}$$

The parameters of *t*, *a*, *r/a*, and *w* of *1D PhC NB* are 200 nm, 400 nm, 0.35, and 1.2*a* respectively. The simulated wavelength in Fig. 3-4(a) shows a blue shift when *P* increases and then saturates when *P* > 30. In addition, in Fig. 3-4(b), both *Q* and *V* increase with *P*. In *1D PhC BE* laser, without the photonic band gap (*PBG*) confinement one of the main optical losses comes from the finite *PhCs* along the *NB*. When *P* increases, this loss is significantly reduced. And this results in the increase of *Q*. Moreover, because the *BE* mode is an extended mode, it is reasonably that the *V* increases with *P*.

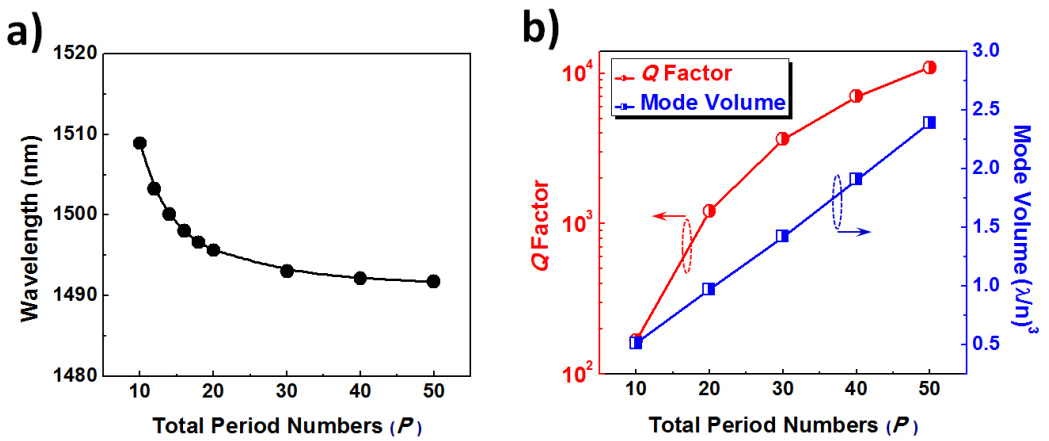


Fig. 3-4: Theoretical (a) wavelength, (b) *Q*, and *V* of the dielectric mode as a function of *P* in *1D PhC NB* on $SiO_2$.

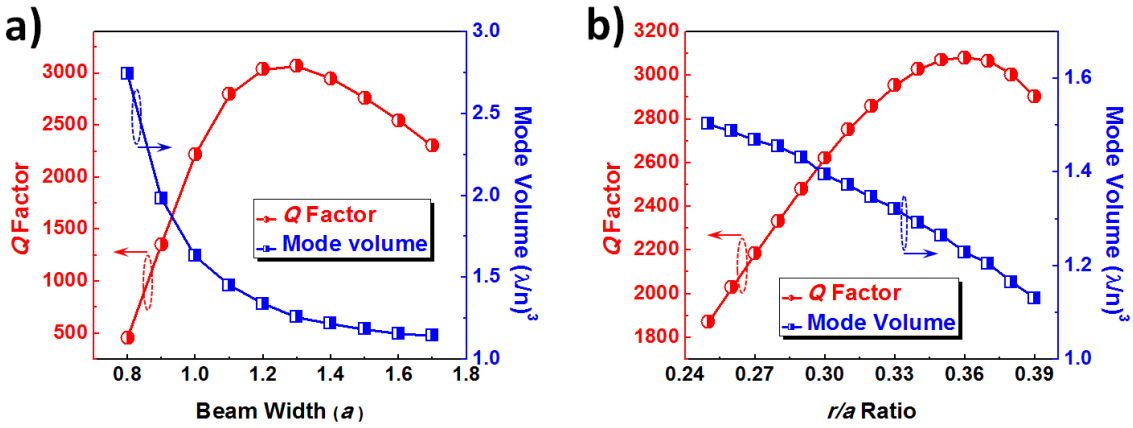


Fig. 3-5: Theoretical $Q$ and $V$ as a function of (a) beam width $w$ (with fixed $r/a$ = 0.35) and (b) $r/a$ ratio (with fixed $w$ = 1.3$a$), while $t$, $a$, and $P$ are fixed at 200 nm, 400nm, and 28 respectively.

We then further investigate the influence of different beam width $w$ and $r/a$ ratio on $Q$ and $V$ individually. At first, with fixed $t$, $a$, $r/a$, and $P$ of 200 nm, 400 nm, 0.35, and 28, there is an optimized $Q$ value of ~ 3,070 when $w$ = 1.3$a$, as shown in Fig. 3-5(a). Two mechanisms are responsible for this optimization. First, when $w$ is smaller than 1.3$a$, more fields in the *NB* penetrate into the air region, thus decreases the $Q$ values. Second, when $w$ becomes larger than 1.3$a$, the photonic band becomes steep and the group velocity at $k_x$ = 0.5 will increase. Increased group velocity means reduced slow light effect and leads to decreased $Q$. In addition, $V$ decreases because the mode field concentrates more inside the *NB*.

Moreover, with fixed $t$, $a$, $w$, and $P$ of 200 nm, 400 nm, 1.3$a$, and 28, theoretical $Q$ and $V$ under different $r/a$ ratios are shown in Fig. 3-5(b). An optimal $Q$ ~ 3,100 can be obtained when $r/a$ = 0.36. There are also two mechanisms responsible for this optimal value. The first one is that the group velocity at $k_x$ = 0.5 becomes higher when $r/a$ ratio decreases, which leads to the decreased $Q$. The other one is that the effective index of *NB* decreases when $r/a$ ratio increases, which leads to weakened *TIR* effect responsible for the decreased $Q$. And the theoretical $V$ is about 1.2 $(\lambda/n_{InGaAsP})^3$ when $r/a$ = 0.36, which is attributed to the extended mode feature of the *BE* mode.

### 3.3.2 *1D PhC NB BE* Lasers on $SiO_2$ Substrate

In experiments, Fig. 3-6 shows the top-view *SEM* picture of a fabricated *1D PhC NB* on $SiO_2$ substrate. The underlying $SiO_2$ can be clearly observed in the inset. The parameters *t*, *r/a*, *P*, and *w* are 200 nm, 0.29, 28, and 1.27*a* respectively. With these parameters, the theoretical *Q* value of the dielectric mode is about 2,500, which is sufficient for lasing. The device footprint area of *1D PhC NB* laser is about 23.5 $\mu m^2$, which is much smaller than 219 $\mu m^2$ in *2D* square-*PhC* laser shown in Fig. 3-1. It is worthy to note that the distributed Bragg reflectors (*DBRs*) applied in *1D PhC NB*s in Fig. 3-6 is the dummy patterns for proximity correction during e-beam lithography to avoid the pattern non-uniformity along the *NB*. Fig. 3-7(a) shows the *SEM* image of *1D PhC NB* on $SiO_2$, where the air-windows are directly defined. Exposing the large area needs large dosage in *e*-beam lithography, which leads to distortion in beam shape and non-uniform in the air-hole radii along the *NB*. Moreover, adding the *DBR*s will not significantly affect the dielectric modal properties in *1D PhC NB*. To confirm this, we calculate the resonant wavelengths and *Q* factors of the dielectric modes under three different situations, including *NB* without *DBRs*, *NB* with ideal *DBRs* for 1550 nm, and *NB* with *DBRs* with parameters in fabrications. The simulation results are shown in Fig. 3-7. Under these three different situations, we find that there are very little differences in mode profile, resonant wavelength, and theoretical *Q* factor. The dielectric mode we focus is a well-propagating wave along the *NB* ($k_x$ = 0.5), that is, y-component of the wave vector is

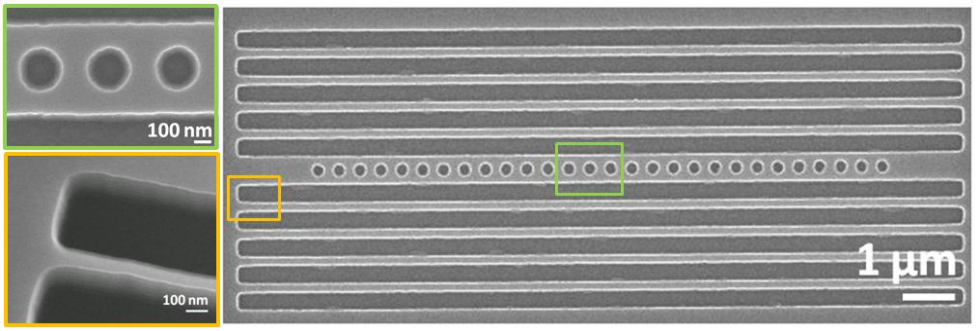


Fig. 3-6: Top- and tilted-view *SEM* pictures of *1D PhC NB* with *P* of 28 on $SiO_2$ substrate.

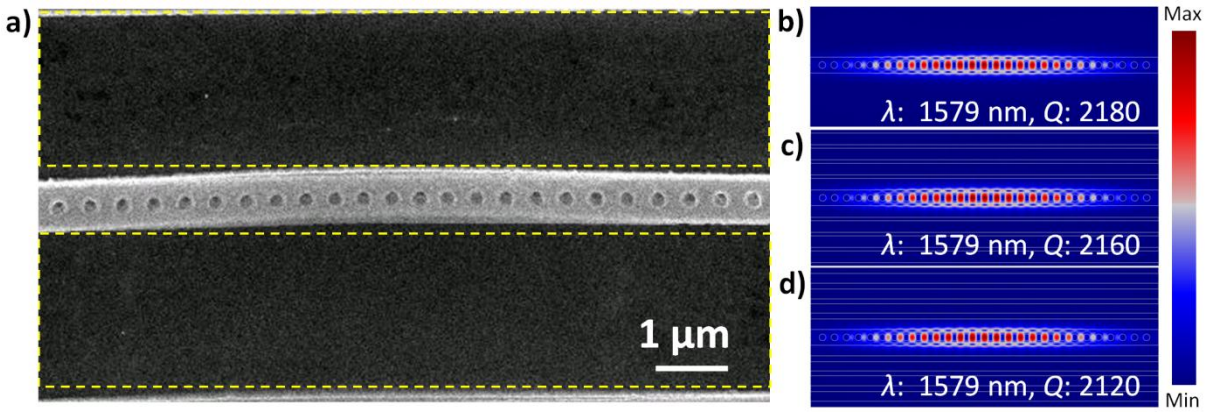


Fig. 3-7: (a) *1D PhC NB* on $SiO_2$ substrate with directly defined air-windows shows significant distortion in *NB* shape. Theoretical mode profile in electric fields of dielectric mode in *1D PhC NB* on $SiO_2$ (a) without *DBRs*, (b) with ideal *DBRs* for 1550 nm, and (c) with *DBRs* with parameters in fabrications. The parameters *t*, *r/a*, *w*, and *P* of *1D PhC NB* are 180 nm, 0.28, 1.31*a*, and 28. Theoretical wavelengths and *Q* factors of the three situations are almost the same.

almost zero. Therefore, the *DBRs* along *y*-direction will not affect such a wave. In measurements, in Fig. 3-8(a), the single-mode lasing spectra at 1486 nm shows *SMSR* > 25 dB. In Fig. 3-8(b), unlike the emission from *2D* square-*PhC BE* laser shown in

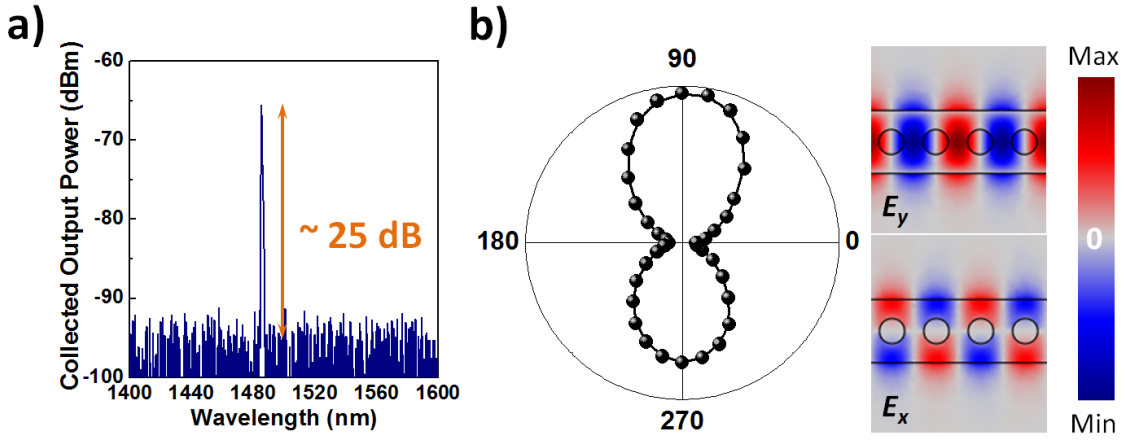


Fig. 3-8: Measured single-mode lasing spectrum at 1486 nm shows *SMSR* > 25 dB under pump power of 7 mW. (b) The measured emission shows linear polarization with polarized ratio of 10.9, owing to the dominated $E_y$ field of the dielectric mode in *1D PhC NB*, as shown by the insets.

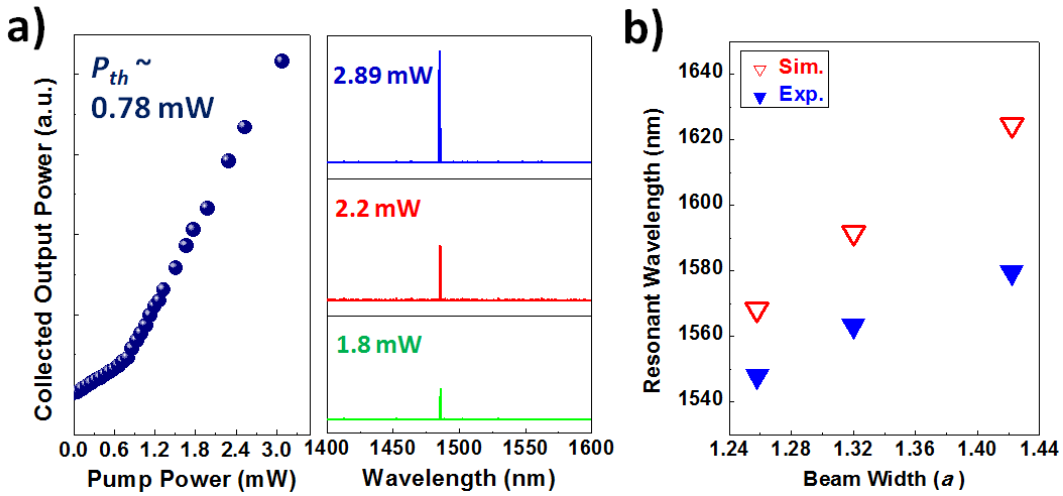


Fig. 3-9: (a) A threshold power of 0.78 mW is obtained from the *L-L* curve. The inset shows the lasing spectra under different pump power to confirm the single-mode lasing. (b) Wavelength matching between the measurement and *3D FEM* simulation results of the dielectric mode in *1D PhC NB BE* lasers with fixed *t*, *a*, and *r/a* ratio of 200 nm, 400 nm, and 0.31 under different *w*.

Fig. 3-2(d), the *BE* laser emission form *1D PhC NB* shows *y*-polarization with polarized ratio of 10.9. This is because the dielectric mode in *1D PhC NB* is dominated by $E_y$ field, as shown in the inset of Fig. 3-8(b). A threshold value of 0.78 mW is obtained from the *L-L* curve shown in Fig. 3-9 (a), which is higher than that of *1D PhC NB BE* laser based on slab structure reported by S. Kim *et al.* [26] owing to the underlying lossy $SiO_2$. In addition, considering the power absorbed by the *InGaAsP MQW*s and overlaps between the pump spot and *PhC* device, the effective threshold is estimated to be 27 μW. However, 0.78 mW is much lower than the threshold (~ 4.25 mW) of *2D* square-*PhC BE* laser shown in Fig. 3-2(b). Under the similar *Q* factors, this improvement in threshold is mainly attributed to the greatly reduced device footprint of *1D PhC NB BE* laser. In addition, lasing spectra under different pump power from 1.8 mW to 2.89 mW are also shown as the inset of Fig. 3-9(a) to confirm the single-mode lasing.

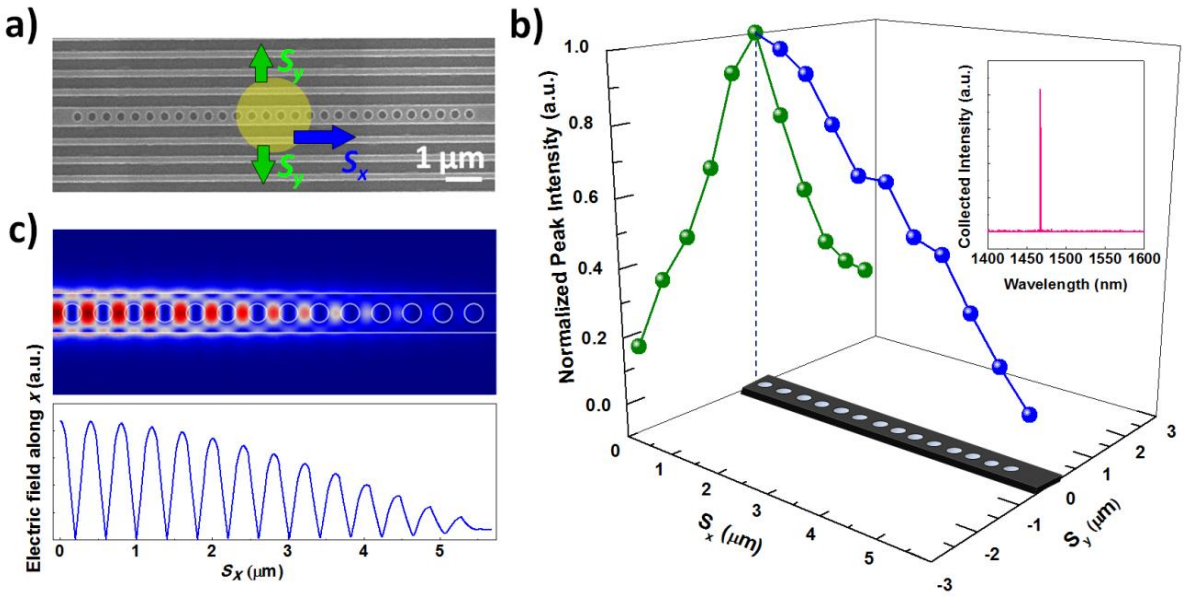


Fig. 3-10: (a) *SEM* picture of *1D PhC NB BE* laser on $SiO_2$ and scheme of pump spot shifting. (b) Normalized laser emission intensities under different pump spot position from the center of *NB* along *x*- and *y*-directions. (c) Theoretical mode profile in electric field of the dielectric *BE* mode in *1D PhC NB* and its extended electric field distribution along the cross-line of the *NB* in *x*-direction.

To identify the lasing mode as the dielectric *BE* mode, the measured lasing wavelengths and *3D FEM* simulated dielectric mode frequency of *1D PhC NB* with different beam widths *w* are shown in Fig. 3-9(b). The results match with each other and both show red shifts owing to the increase of effective index of the *NB* when the beam width increases. Therefore we can initially identify the lasing mode as the dielectric mode. The difference between simulated and measured lasing wavelength may come from the fabrication imperfection, thickness variation of *MQW*s, refractive index of $SiO_2$ layer ($n_{SiO2}$ = 1.44 in our simulation), value estimated from *SEM* pictures, and so on.

Furthermore, to confirm the extended mode distribution of the dielectric lasing mode in *1D PhC NB BE* laser, we shift the pump position along *x*- and *y*-directions individually to explore the excitation map of the lasing mode, as shown in Fig. 3-10(a). The pump power and spot size are fixed at 5.5 mW and 6 μm in diameter. The single-mode lasing spectrum at 1466 nm of the characterized device is shown as the inset of Fig. 3-10(b). As illustrated in Fig.

3-10(a), at first, the pump spot is move away from the center of the *NB* in *x*-direction. The intensities of lasing emission under pump spot shift $S_x$ from 0 to 6 μm are shown in Fig. 3-10(b). The intensity at $S_x$ = 3.2 μm decreases to be half of that at $S_x$ = 0. Lasing actions are no longer observed when $S_x$ > 5.5 μm. This broad intensities variation at different $S_x$ is obviously different from the localized excitation map of the localized defect mode in *PhC* nanocavities, which agrees with the theoretical extended electric field distribution of the dielectric *BE* mode shown in Fig. 3-10(c). In Fig. 3-10(c), with parameters *t*, *w*, *r/a*, *a*, and *P* of 200 nm, 1.27*a*, 0.3, 400 nm, and 28, the electric field of the dielectric *BE* mode in *1D PhC NB* along the cross-line is spread from 0 to 5.6 μm. This broad electric field distribution will lead to the lasing behavior can even be observed when $S_x$ = 5.5 μm. Thus, we can confirm the lasing mode as the dielectric *BE* mode again. In addition, we also show the lasing emission intensity variation when the pump spot size is move away from the center of *NB* along *y*-direction, as shown in Fig. 3-10(b). Lasing actions cannot be observed when the shift is larger than 2.7 μm, while the pump spot is out of overlapping with the *NB*.

Unlike the fragile suspended slab structure, asymmetric structure provides a stable mechanical supporting. In a suspended *1D PhC NB*, large *P* over 30 may lead to the *NB* bending or collapse [30]. However, constructing *1D PhC NB* on asymmetric structure can avoid these issues. To emphasize this, in the following experiment, we demonstrate a *1D PhC BE NB* laser with *P* = 36 on $SiO_2$ substrate. The top-view *SEM* picture of the characterized device is shown in Fig. 3-11(a), which is with parameters *t*, *w*, *a*, and *r/a* ratio of 200 nm, 1.39*a*, 400 nm, and 0.29 and has theoretical *Q* factor of $4.69 \times 10^3$ via *3D FEM* simulation. The measured single-mode lasing spectrum at 1491 nm and *L-L* curve are also shown in Fig. 3-11(b) and (c). A lower threshold value (~ 0.6 mW and effective threshold of 21 μW) than that (~ 0.78 mW and effective threshold of 27 μW) of *NB* with *P* = 28 can be obtained from the *L-L* curve, which comes from the higher *Q* value owing to the better slow light effect under large *P*.

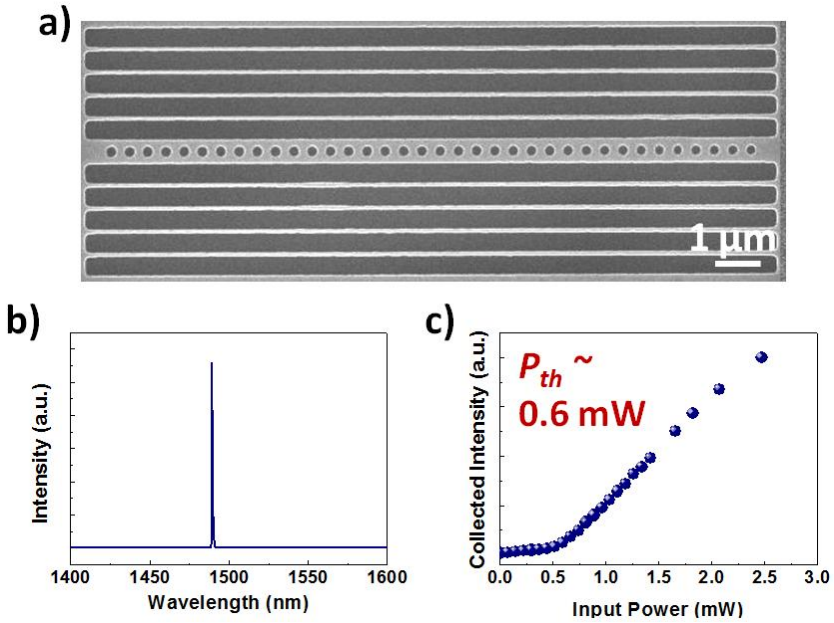


Fig. 3-11: (a) Top-view *SEM* picture, (b) single-mode lasing spectrum, and (c) *L-L* curve of *1D PhC NB BE* laser with $P$ = 36. The *L-L* curve shows a low threshold power of 0.6 mW. The parameters *t*, *w*, *a*, and *r/a* ratio are 200 nm, 1.39*a*, 400 nm, and 0.29 respectively.

## 3.4 Summary

In this chapter, we have demonstrated *2D* square-*PhC* and *1D PhC NB BE* lasers on $SiO_2$ substrate and discuss their lasing properties both in simulations and experiments. Lasing threshold of 4.25 mW from the $M_1$ *BE* mode and device footprint of 14.8 × 14.8 μm$^2$ in *2D* square-*PhC BE* laser on $SiO_2$ are both worse than those (threshold of 0.78 mW and device footprint of 11.2 × 2.1 μm$^2$ of *1D PhC NB BE* lasers with $P$ = 28 on $SiO_2$, which show the benefits of *1D PhC NB BE* lasers as the light source in condensed photonic integrated circuits. In addition to the frequency matching, varying the pump spot position is used to confirm the extended feature of the dielectric *BE* lasing mode. Moreover, we also increase the $P$ to be 36 to obtain a lower threshold of 0.6 mW, while also prove the mechanical stability of constructing *1D PhC NB* device on asymmetric structure.

# Chapter 4

# *1D* Photonic Crystal Lasers Based on Ring Resonator on $SiO_2$ Substrate

## 4.1 Introduction

Two-dimensional (*2D*) photonic crystal ring resonators (*PhCRRs*) [48] show outstanding integralities in constructing versatile photonic integrated circuits (*PICs*) via proper bus *PhC* waveguides. Owing to the *2D* photonic band-gap effect, light recycled propagation can be allowed in *2D PhCRRs* with compact ring sizes, which can be utilized in efficient lasers [40, 41] for *PICs*. In addition to lasers, various function devices based on *2D PhCRRs*, such as add-drop filters [42], logical units [43], and optical buffer [44] have also been proposed and/or demonstrated recently. However, *2D PhCs* will lead to large device footprint and the flexibilities of coupling / integration scheme are restricted by the *PhC* lattice structures. Although one can utilize the design of micro-disk (*MDs*) with different circular periodic nanostructure arrangement [45, 46] to overcome these two drawbacks, the high order modes in *MDs* are still blemished in serving as lasers. Based on the one-dimensional (*1D*) *PhCs* nanobeam (*NB*) band edge laser investigated in chapter 3, a feasible solution is utilizing *1D PhCs NB* to encircle the *1D PhC NB*. Unlike the *2D PhCRR*, *1D PhCRR* has very small device footprint and high flexibility in integration/coupling scheme via side-coupled ridge waveguides in *PICs* without lattice structure restrictions. Furthermore, comparing with traditional ring resonators, *PhCRRs* can control the mode properties via fine-tuning *PhCs* and have strong vertical emissions. In this chapter, compact lasers based on *PhCRRs* will be investigated in simulations and experiments. In chapter 4.2, *1D PhCRR* lasers on $SiO_2$ substrate are demonstrated. In chapter 4.3, a mode-gap confined nanocavity in *1D PhCR* with smaller mode volumes and lower thresholds than *1D PhCRR* will be proposed and investigated.

## 4.2 *1D PhCRR* Lasers on $SiO_2$ Substrate

*1D PhCRR* can be formed by encircling *1D PhC NB*, thus the dielectric mode propagation shown in chapter 3 can recycle in such resonator with ultrasmall device footprint. Scheme of a *1D PhCRR* based on *InGaAsP MQW*s with underlying $SiO_2$ substrate is shown in Fig. 4-1 (a). The important parameters, including thickness of *InGaAsP MQW*s ($t$), ring width ($w$), air-hole radius ($r$), radius of ring resonator ($R$), lattice constant ($a$), total period numbers ($P$), refraction indices of *InGaAsP MQW*s ($n_{InGaAsP}$) and $SiO_2$ ($n_{SiO2}$) are also defined in Fig. 4-1 (a) and (b). Theoretical dielectric mode profile in electric fields in *1D PhCRR* with $P$ = 28 via *3D FEM* is shown in Fig. 4-1 (c). The lasing mode azimuthal number of 14 is determined by $P$ = 28.

### 4.2.1 Dielectric Mode Properties in *1D PhCRR*

To understand the dielectric mode behaviors in *1D PhCRR*, at first, we calculate the $Q$ and confinement factor $\gamma_d$ as function of total period numbers when $t$, $w$, and $r/a$ ratio are

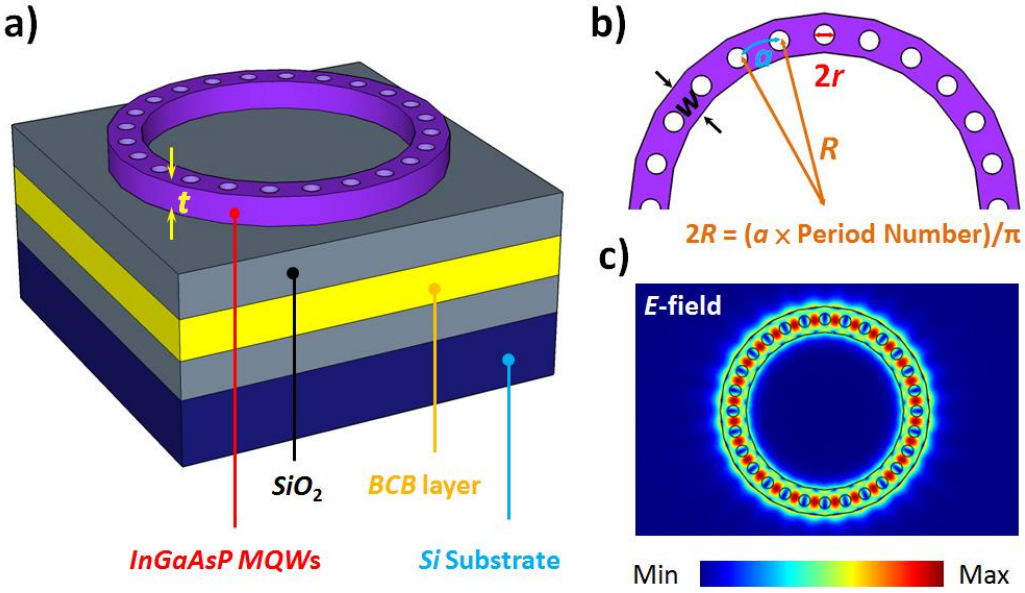


Fig. 4-1: (a) Scheme of *1D PhCRR* on $SiO_2$ substrate and (b) definitions of important parameters. (c) Theoretical mode profile in electric field of *1D PhCRR* with $P$ = 28 via *3D FEM*.

fixed at 190 nm, 1.3*a*, and 0.28, as shown in Fig. 4-2 (a). The $\gamma_{di}$ is defined as the ratio of total energy in dielectric region and expressed as:

$$\gamma_d = \frac{\int_{dielectric} |E|^2 dV}{\int_{total} |E|^2 dV} \tag{4-1}$$

In Fig. 4-2 (a), both of $Q$ and $\gamma_d$ increase with $P$. This is because the increase of $P$ will enlarge the ring size, thus reduces the bend loss and leads to the increase of $Q$. And the $\gamma_d$ increases with $Q$ monotonically. To keep the device footprint of *1D PhCRR* small, $P$ is chosen as 28 in the following simulations, while $Q$ is about $10^4$. And then we investigate the influence of $w$ on

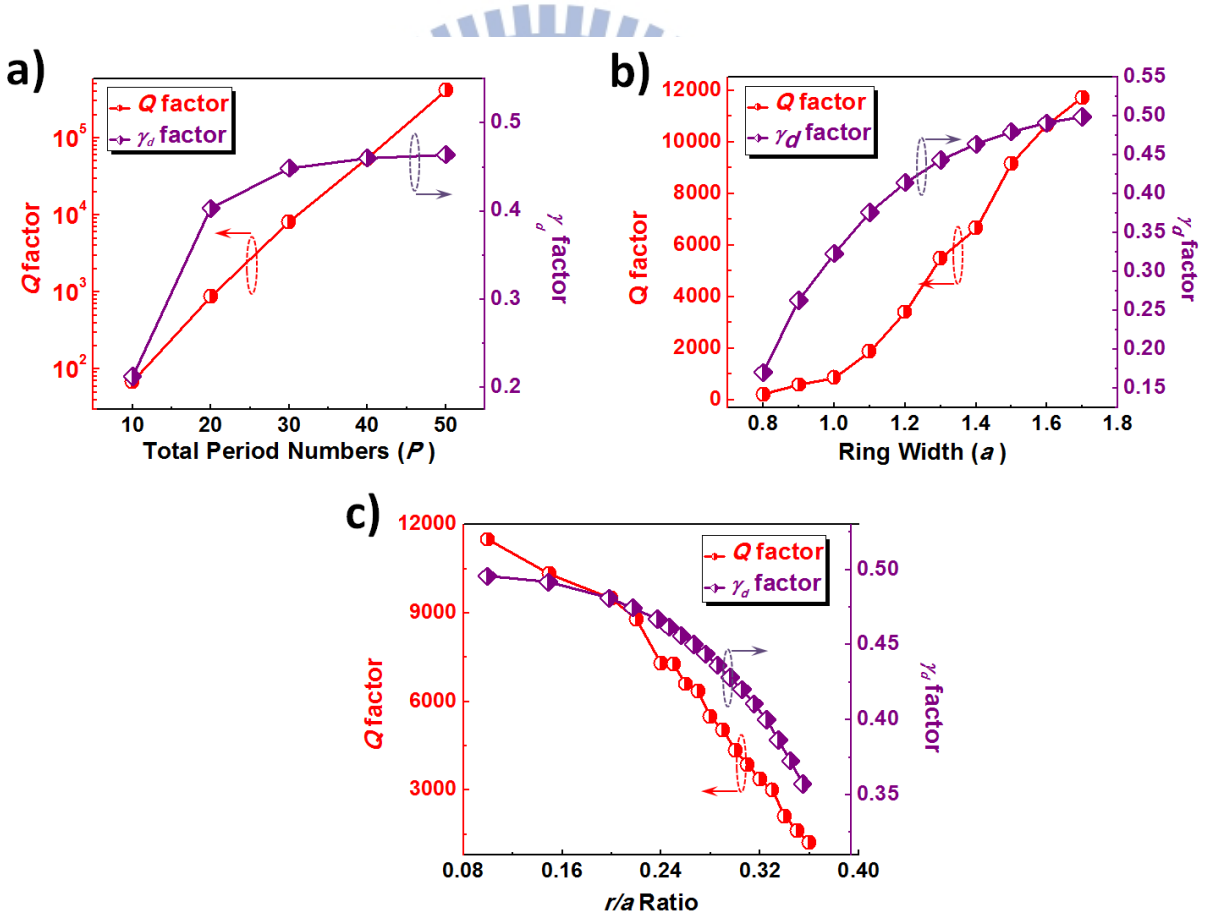


Fig. 4-2: (a) Theoretical $Q$ and $\gamma_d$ factors of *1D PhCRR* as a function of $P$ form 10 to 50 with fixed $w$ and $r/a$ ratio of 1.3$a$ and 0.28. (b) Theoretical $Q$ and $\gamma_d$ factors as a function of $w$ with fixed $P$ and $r/a$ ratio of 28 and 0.28. (c) Theoretical $Q$ and $\gamma_d$ factors of *1D PhCRR* as a function of $r/a$ ratio with fixed $P$ and $w$ of 28, and 1.3$a$. The parameters $t$ and $a$ are fixed at 190 and 400 nm in (a)-(c).

*Q* and $\gamma_d$ of *1D PhCRRs* as shown in Fig. 4-2 (b). The parameters of *t* and *r/a* ratio are fixed at 190 nm and 0.28 in simulations. An optimal $Q \sim 1.17 \times 10^4$ occurs when $w = 1.7a$ and two mechanisms are responsible for this. The first one is that the effect index becomes higher as *w* increases, thus *Q* increases. The second one is that the high-order mode appears when *w* is larger than 1.7*a*, while *Q* starts to decrease. In addition, the $\gamma_d$ factor increases with width owing to the increased effective index. Furthermore, the theoretical *Q* and $\gamma_d$ of *1D PhCRR* as function of *r/a* ratio under parameters *t*, *a*, and *w* of 190 nm, 400 nm, and 1.3*a*, are shown in Fig. 4-2 (c). Both of them decrease as the *r/a* ratio increases. This is caused by the decrease of effective index of *1D PhCRR* owing to the increased *r/a* ratio.

### 4.2.2 Measurement Results of *1D PhCRR* Lasers on $SiO_2$ Substrate

To keep small device footprint and sufficient *Q* for lasing simultaneously, *P* of the characterized devices is chosen as 28 in the following experiments, while the ring radius *R* and device footprint is only 1.78 μm and 30 $\mu m^2$. Top- and tilted-view *SEM* pictures of a *1D PhCRR* with surrounded distributed Bragg reflectors (*DBRs*) are shown in Fig. 4-3(a) and (b). In the tilted-view *SEM* picture, underlying $SiO_2$ layer can be clearly observed. The parameters *t*, *a*, *r/a* ratio, and *w* of the fabricated *1D PhCRR* are 190 nm, 400 nm, 0.28, and 1.28*a*. As we mentioned in chapter 3.3.2, this *DBRs* is used to reduce the proximity effect during electron beam lithography without significantly affecting the modal properties of *1D PhCRR*. To confirm this, we simulate the wavelengths, *Q* factors, and mode profiles without/with different *DBR* structure. In Fig. 4-3(c) - (e), simulated mode profiles in electric-field of these three conditions are very similar to each others. In addition, the central wavelengths show no difference between these three conditions. Although there is 7% difference of *Q* factors between *1D PhCRRs* with perfect and fabricated *DBRs*, they are still in the same orders with that without *DBRs*. Moreover, we can not find a mode utilizing *DBR*s as mirror in the range ranging from 1400 nm to 1600 nm in simulation. Therefore, the measured mode is a

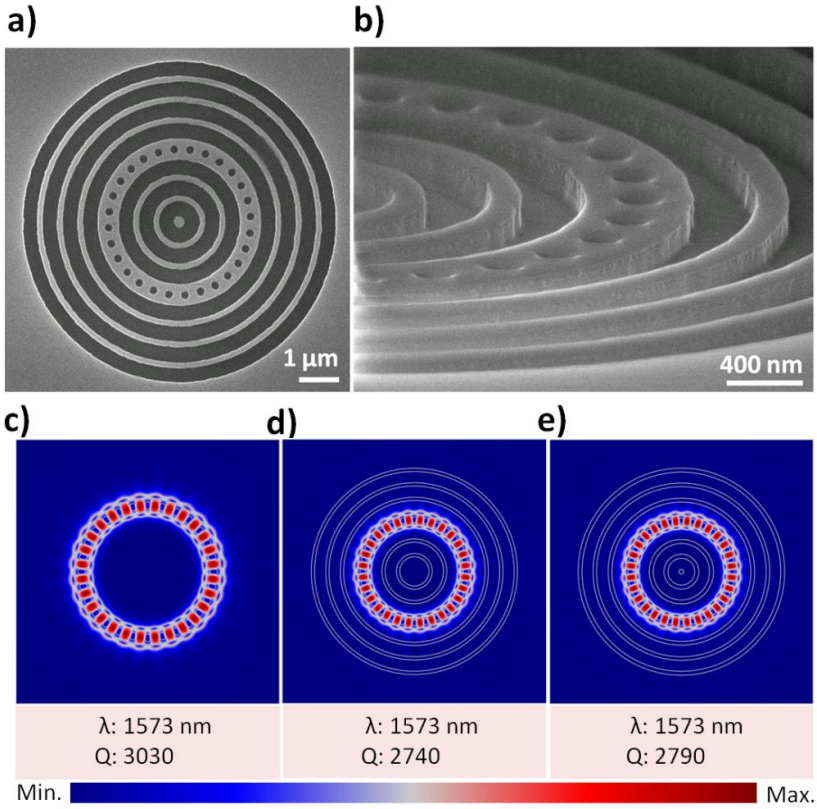


Fig. 4-3: (a) Top- and (b) tilted-view *SEM* pictures of *1D PhCRR* with $P$ = 28. Underlying $SiO_2$ substrate can be clearly observed in (b). Theoretical mode profiles in electric fields of *1D PhCRR* (c) without *DBR*s, (d) with ideal *DBRs* for 1550 nm, and (e) with *DBRs* in fabrications. The parameters $t$, $r/a$ ratio, $w$, and $P$ of *1D PhCRR* are 160 nm, 0.25, 550 nm, and 28. The theoretical wavelengths and $Q$ factors of *1D PhCRRs* in (c)-(e) are denoted and almost the same.

propagation mode in *1D PhCRR* as shown in Fig. 4-1(c).

In measurements, the pump spot size is large enough (about 6 μm in diameter) to cover the whole *1D PhCRR*s and results in sufficient carrier injection. The single mode lasing spectrum at 1523 nm from *1D PhCRR* on $SiO_2$ substrate is shown in Fig. 4-4 (a), which shows a side-mode suppression-ratio (*SMSR*) of 26 dB. A threshold power of 0.7 mW and effective threshold of 47 μW can be estimated from the measured light-in light-out (*L-L*) curve shown in Fig. 4-4(b). In the inset of Fig. 4-4(b), the polarization with low polarized ratio of 1.94 agrees with the circular distribution of the mode profile of *1D PhCRR* on $SiO_2$, that is, neither $E_x$ nor $E_y$ fields dominate the mode. We believe that the ideal polarization should be un-polarized. The slightly-polarized degree can be attributed to the fabrication imperfection of

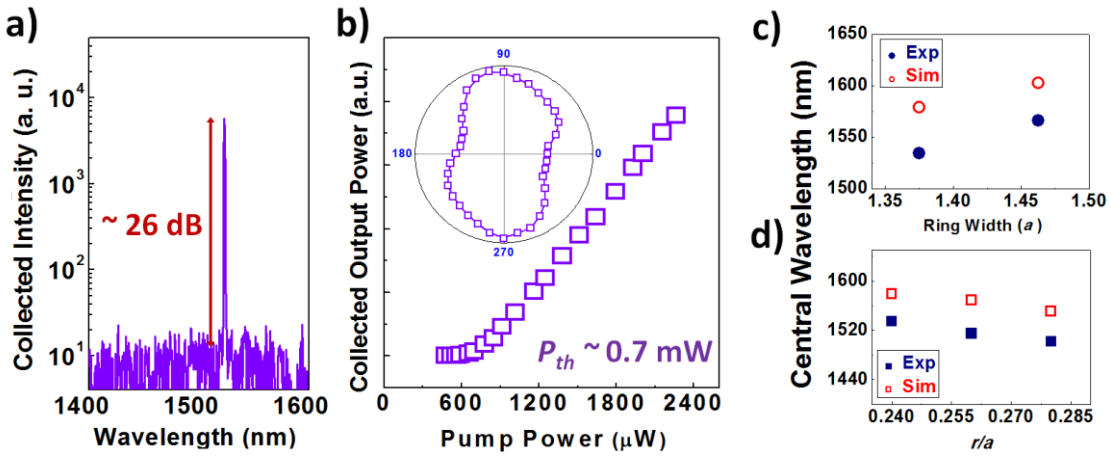


Fig. 4-4: (a) Single mode lasing spectrum from *1D PhCRR* on $SiO_2$ substrate with lasing wavelength of 1523 nm and *SMSR* of 26 *dB*. (b) The *L-L* curve and the inset polarization show a threshold power of 0.7 mW and low polarized degree of 1.94. Theoretical and measured lasing wavelengths of *1D PhCRR* with (c) different *w* and (d) *r/a* ratios on $SiO_2$.

the characterized device.

To further identify the lasing mode in *1D PhCRR* on $SiO_2$ as the dielectric mode shown in Fig. 4-1(c), various devices with fixed *w* and *r/a* ratios are characterized. With fixed *t*, *a*, *r/a* ratio, and *P* of 160 nm, 400 nm, 0.24, and 28, Fig. 4-4(c) shows the measured and theoretical lasing wavelengths of *1D PhCRRs* with different *w*. The measured lasing wavelength shows a red shift owing to the increase of effective index when *w* increases, which agree with the theoretical wavelengths of dielectric mode via *3D FEM*. Furthermore, with fixed *t*, *a*, *w*, and *P* of 160 nm, 400 nm, 1.36*a*, and 28, with different *r/a* ratio, the measured and theoretical lasing wavelengths of *1D PhCRRs* with different *r/a* ratio shown in Fig. 4-4(d) also show good match with each other. The lasing wavelength shows a blue shift owing to the reduced effective index when the *r/a* ratio increases.

To find the minimum ring size for lasing, *1D PhCRR*s on $SiO_2$ with different *P* from 20 to 36 are characterized. The measured lasing wavelength as a function of *P* is shown in Fig. 4-5(a), where the lasing action can be still observed when *P* = *24*. When *P* = 24, the ring diameter and device footprint is only 3 μm and 25.5 $\mu m^2$. The lasing spectrum and *SEM*

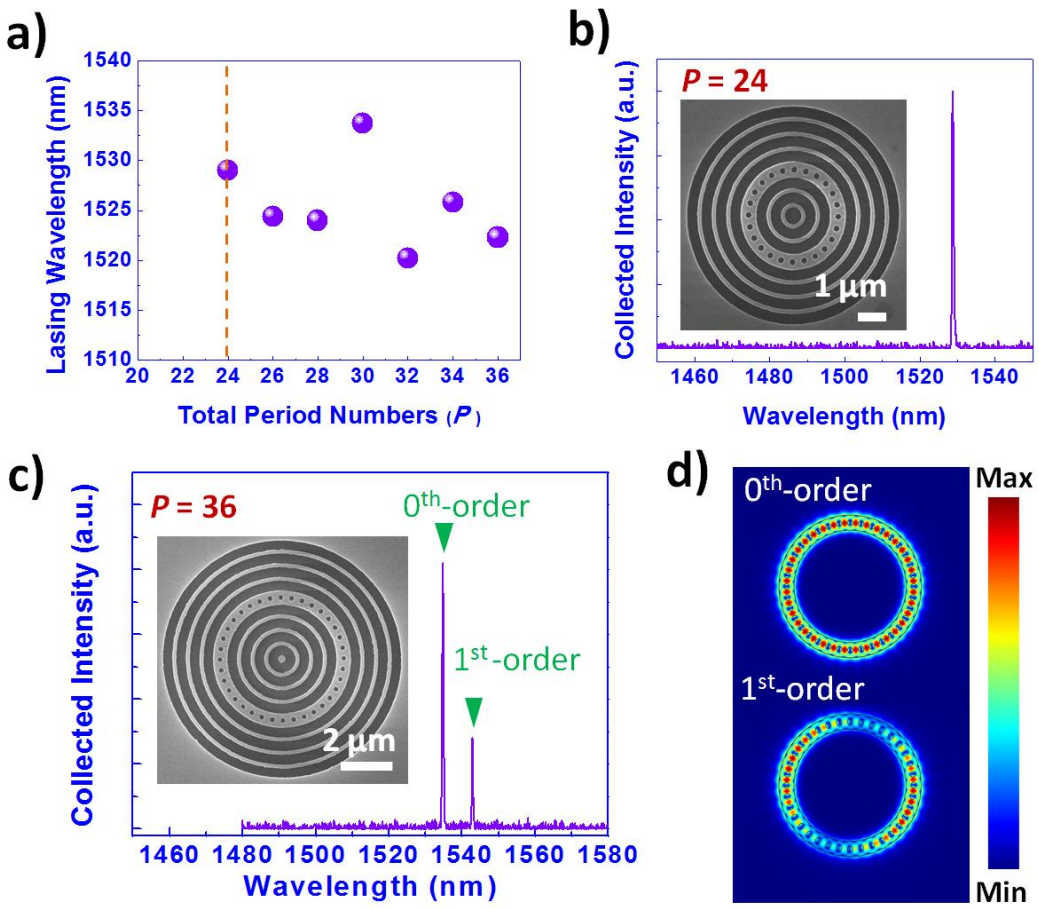


Fig. 4-5: (a) The measured lasing wavelength from *1D PhCRRs* on $SiO_2$ with different *P*. Lasing action can be still observed when $P = 24$. (b) Single-mode lasing spectrum and *SEM* picture of *1D PhCRR* on $SiO_2$ with $P = 24$. (c) The $0^{th}$- and $1^{st}$-order modes can be observed in spectrum simultaneously when *P* increases to be 36. The measured wavelength difference is 8.1 nm. (d) Theoretical mode profiles in electric fields of the $0^{th}$- and $1^{st}$-order modes. The theoretical wavelength difference is 9.2 nm.

picture of *1D PhCRR* on $SiO_2$ with $P = 24$ are shown in Fig. 4-5(b) and its inset. In addition, as shown in Fig. 4-5(a), the wavelength fluctuation under different *P* is about ± 7 nm. Although those *1D PhCRRs* are designed with the same parameters, the fabrication imperfections originated from electron beam lithography and *ICP* dry etching in *w* and *r* may cause this wavelength fluctuation. However, when *P* increases to be 36, the $1^{st}$-order mode lasing can be observed. Fig. 4-5(c) shows the multi-mode lasing spectrum and *SEM* picture of *1D PhCRR* on $SiO_2$ with $P = 36$. The appearance of high order mode is owing to its increased *Q* with *P*. This multi-mode lasing spectrum is also confirmed by *3D FEM* simulation. The

theoretical mode profiles of $0^{th}$- and $1^{st}$-order modes in electric fields are shown in Fig. 4-5(d). The measured wavelength difference of 8.1 nm in Fig. 4-5(c) agrees with the result (~ 9.2 nm) in simulations.

## 4.3 Mode-Gap Confined Nanocavity Lasers in *1D PhCR* on $SiO_2$ Substrate

Since the *PhC* ring (*PhCR*) provides more flexibility for integrating in *PICs*, we are curious about "can we realize a localized nanocavity on it or not?" Actually, the *1D PhCR* can be regarded as a deformed *1D PhC* nanobeam (*NB*), that is, a bent *1D PhC NB*. It is possible to design a nanocavity on it for laser. However, the deformation (bending) also induces extra loss compared with nanocavity in *1D PhC NB*. In this section, we design a mode-gap confined nanocavity to see its possibility for lasing.

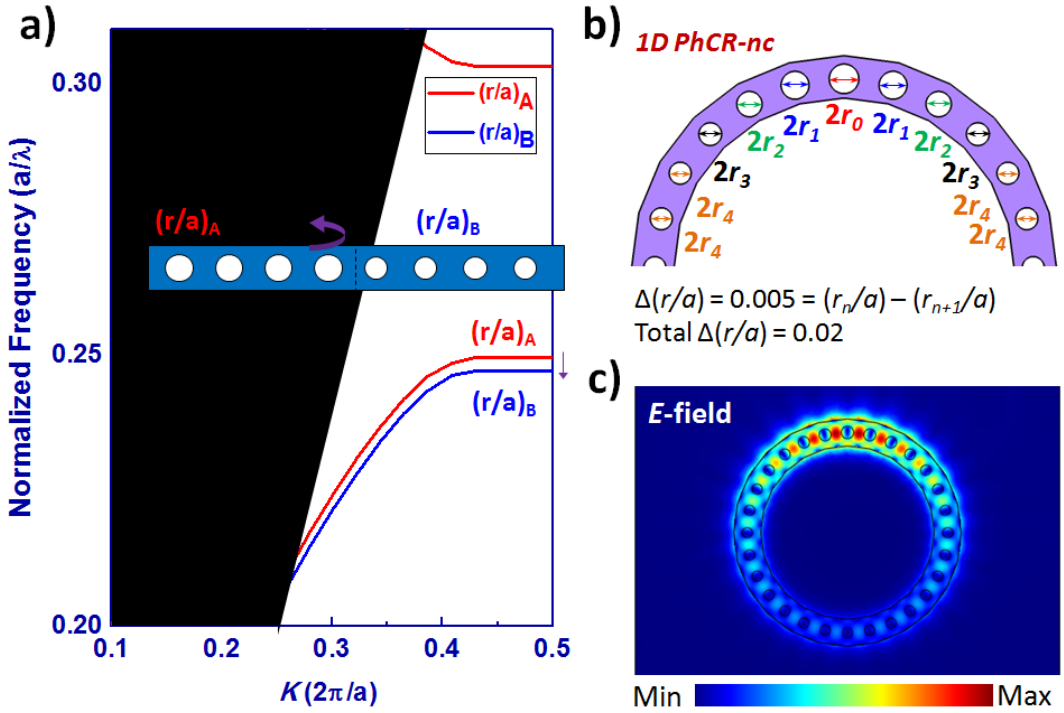


Fig. 4-6: (a) Illustration of mode-gap confinement mechanism via *1D PhC NBs* with different *r/a* ratios. (b) Mode-gap confined *1D PhCR-nc* is achieved by continuously tuning the air-hole radii. (c) Theoretical mode profile in electric field of the confined dielectric mode in *1D PhCR-nc*.

### 4.3.1 Design of Mode-Gap Confined Nanocavity in *1D PhCRR*

The nanocavity design in *1D PhCR* utilizes mode-gap effect. The concept of mode-gap effect is illustrated in Fig. 4-6(a) via *1D PhC NB* with different *r/a* ratios. For a *NB* with *1D* $PhC_A$ and $PhC_B$ with $(r/a)_A$ and $(r/a)_B$ ( $(r/a)_A > (r/a)_B$ with fixed *a*), the frequency of dielectric band in $PhC_A$ is higher than that in $PhC_B$. It means the dielectric mode propagation in $PhC_A$ will be forbidden in $PhC_B$ and reflected at the interface between $PhC_A$ and $PhC_B$. Therefore, the interface between $PhC_A$ and $PhC_B$ forms a mode-gap mirror and double interfaces form a nanocavity. Base on this mode-gap effect, as shown in Fig. 4-6(b), a *1D PhCR* nanocavity (*PhCR-nc*) is formed by continuously tuning air-hole radii under fixed *a* of 400 nm. The *r/a* ratio decreases from central to outer region with region 0.02 total *r/a* ratio variation and 0.005 decrement. Theoretical mode profile in electric field of the confined dielectric mode in *1D PhCR-nc* is shown in Fig. 4-6(c). Comparing with *1D PhCRRs in* chapter 3, we obtain a slightly lower *Q* value ~2670 of the dielectric mode in *PhCR-nc*. However, the localized mode profile also leads to a smaller mode volume of 1.06 $(\lambda/n)^3$. For *1D PhCRR* with the same parameters, the theoretical *Q* and mode volume are ~4110 and 2.87 $(\lambda/n)^3$.

### 4.3.2 Lasing from *1D PhCR-nc* on $SiO_2$ Substrate

We then realize the *1D PhCR-nc* design described above. Top-view *SEM* picture of a *1D PhCR-nc* with *P* = 28 are shown in Fig. 4-7. Different air-hole radii inside ($r_0$) and outside ($r_4$) the nanocavity region are also shown as the inset *SEM* pictures of Fig. 4-7.In measurements, the basic lasing properties of *1D PhCR-nc* on $SiO_2$ substrate with *t*, *a*, $r_0/a$, $\Delta(r/a)$, *w* and *P* of 190 nm, 400 nm, 0.28, 0.013, 1.28*a*, and 28 are shown in Fig. 4-8. Fig. 4-8(a) shows the single-mode lasing spectrum at 1535 nm and *SMSR* of 28 *dB* under fixed peak power of 8 mW. The measured *L-L* curve in Fig. 4-8(b) shows threshold of 0.54 mW and effective threshold of 36 μW. Furthermore, in the inset of Fig. 4-8(b), the polarized degree

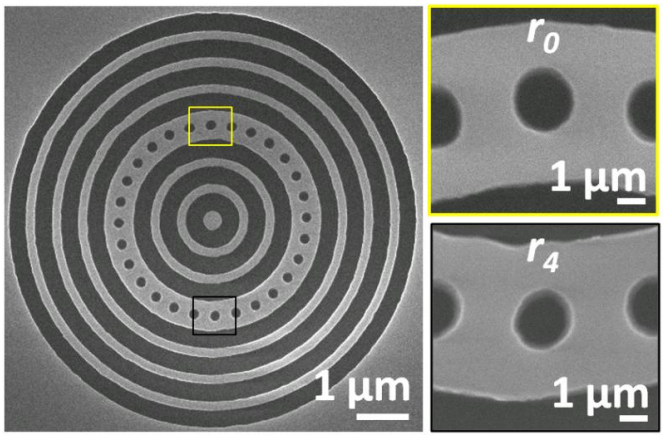


Fig. 4-7: Top-view *SEM* pictures of *1D PhCR-nc* with $P$ = 28. The air-hole radii inside ($r_0$) and outside ($r_4$) the nanocavity region are also shown as the inset *SEM* pictures.

of the laser emissions from *1D PhCR-nc* is 3.14, which is also because neither $E_x$ nor $E_y$ dominate the mode.

Via comparing with the simulation results, we identify the lasing mode from *1D PhCR-ncs* with different $w$ and $r_0/a$ ratios. Fig. 4-8(c) shows the lasing wavelengths of *1D PhCR-nc* with fixed $r_0/a$ of 0.27 and different $w$. The red shift in lasing wavelength is owing to the increased effective index when $w$ increases. Fig. 4-8(d) shows the lasing wavelengths of *1D PhCR-ncs* with fixed $w$ of 1.39$a$ and different $r_0/a$ ratios. The lasing wavelength shows

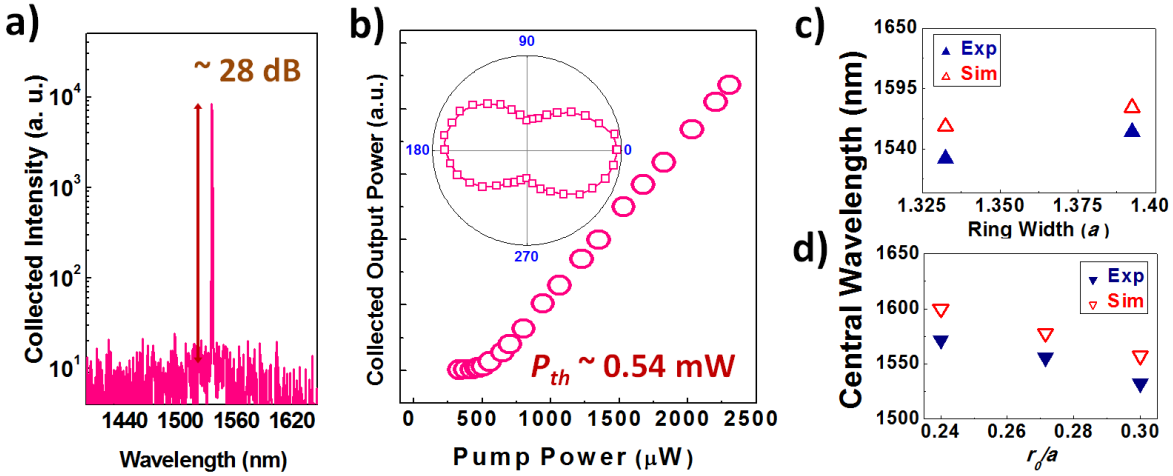


Fig. 4-8: (a) The measured lasing spectrum with lasing wavelength of 1535 nm. The inset shows *SMSR* of 28 dB. (b) The *L-L* curve shows threshold value of 0.54 mW. The inset shows the measured emission with x-polarized ratio of 3.19. Theoretical and measured lasing wavelengths of *1D PhCR-nc* with (c) different $w$ and (d) $r_0/a$ ratios on $SiO_2$.

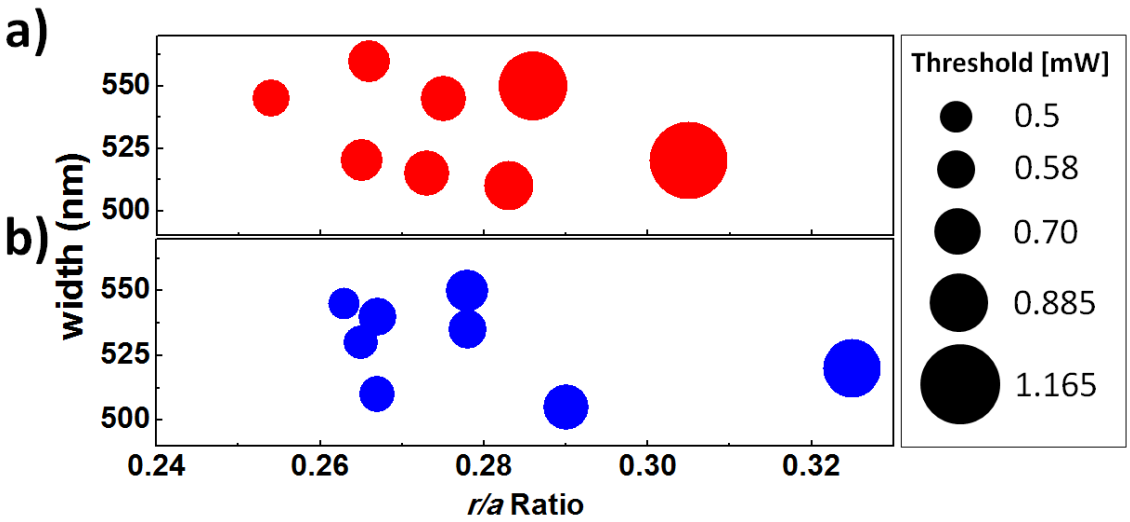


Fig. 4-9: The measured thresholds of *1D* (a) *PhCRRs* and (b) *PhCR-ncs* under different *w* and *r/a*.

blue shift when *r/a* ratio increases, which owing to the decreased effective index. These measurement results agree with the confined dielectric mode in simulation. Thus, we can confirm the lasing mode as the confined dielectric mode shown in Fig. 4-6(c).

Finally, in Fig. 4-9(a) and (b), we show the thresholds of *1D PhCRRs* and *PhCR-ncs* under different *w* and *r/a*. Under the same parameters, we can see that the threshold of *1D PhCRRs* is always higher than that of *1D PhCRC-ncs*. This is owing to the smaller mode volume of *1D PhCRC-ncs* than that of *1D PhCRRs*. And the thresholds of *1D PhCRRs* and *PhCR-ncs* both decrease with *r/a* and increase when *w* decreases, which strongly correlate with the variation of $\gamma_d$ under different *r/a* and *w* shown in Fig. 4-2(b) and (c).

## 4.4 Summary

In this chapter, we have proposed and initially investigated basic lasing properties of *1D PhCRR* and *PhCR-nc* on $SiO_2$ substrate. With $P$ = 28, single-mode lasing with threshold of 0.7 mW and effective threshold of 47 μW from *1D PhCRR* is obtained. The minimum $P$ of *1D PhCRR* for lasing is 24, which leads to a compact ring size of only 3 μm in diameter and device footprint of only 25.5 $\mu m^2$. In addition, for the single-mode lasing from *1D PhCR-nc*,

we further obtain a lower threshold of 0.54 mW and effective threshold of 36 μW and smaller mode volume. This kind of laser based on *1D PhC* ring not only has small device footprint, but also has high flexibility via side-coupled ridge waveguide in condensed *PIC*s.

# Chapter 5

# Summary and Future Works

## 5.1 Summary

In this thesis, via well-established nano-fabrication process of photonic crystals (*PhCs*) and developing *BCB* adhesive bonding techniques, we have transferred *III-V* active epitaxial materials onto $SiO_2$ substrate and realized various *PhC* lasers, including band-edge (*BE*) and cavity lasers, on $SiO_2$ substrate with small device footprints. In addition to fabrication process, the numerical simulation tools and near-infrared micro-photoluminescence systems used to design and characterize the devices have also been introduced in chapter 2.

In chapter 3, we have investigated two-dimensional (*2D*) square-*PhC BE* lasers for reference, which has device footprint of 14.8 × 14.8 $\mu m^2$. Via eliminating *PhCs* in one dimension, we have realized one-dimensional (*1D*) *PhC* nanobeam (*NB*) *BE* lasers on $SiO_2$ substrate. This device shows single-mode lasing with threshold of 0.78 mW, while the device footprint is as small as 11.2 × 2.1 $\mu m^2$ when total *PhC* period number is 28. Because the underlying $SiO_2$ provides excellent mechanical supporting, the structures of *1D PhC NB BE* lasers are very stable even with large *PhC* period number.

In chapter 4, via encircling *1D PhC NB BE* laser on $SiO_2$, a novel *1D PhC* ring resonator (*PhCRR*) has been formed and investigated. The *1D PhCRR* laser shows threshold value of 0.7 mW and low polarized ratio of 1.94. This kind of device also shows small device footprint of 30 $\mu m^2$. In experiments, the minimum *PhC* period for lasing is 24, while the ring size is only 3 μm in diameter. Furthermore, we have designed a mode-gap confined nanocavity on *1D PhCR*. Smaller mode volume ($1.06\ (\lambda/n)^3 < 2.87\ (\lambda/n)^3$) and lower lasing threshold of 0.54 mw than those of *1D PhCRRs* are obtained.

We believe that both *1D PhC NB BE* and *PhCRR* lasers shown in the thesis will be good candidates for compact laser light-sources in photonic integrated circuits (*PICs*). In addition to small device footprints, without lattice structure restrictions, lasers based on *PhCRs* also show good flexibilities for integrating in *PICs* via side-coupled ridge waveguides.

## 5.2 Future Works

In this thesis, although we have realized ultra-compact *PhC* lasers on $SiO_2$ substrate via *BCB* adhesive bonding, these devices are under pulsed operation. *CW* operations of *1D PhC NB BE* and *PhCRR* lasers have not been achieved yet in the present works. To achieve *CW* operations:

1. Roughness of the etched side wall and surface should be improved to reduce the thermal problems caused by non-radiative recombinations.
2. Transferring *III-V* active epitaxial materials onto substrates with better thermal conductivities than $SiO_2$ substrate, for example, $Al_2O_3$.

# Appendix A

## A.1 Device Footprints of Photonic Crystal Devices

In our works, device footprint is defined as the effective area of a photonic crystal (*PhC*) device where the coupling effect can be neglected when there are other devices nearby. Fig. A-1 illustrates the definitions of device footprint of *PhC* devices in this thesis, including two-dimensional (*2D*) square-*PhCs*, *1D PhC* nanobeam (*NB*), and *1D PhC* ring resonator (*PhCRR*). For *1D PhC NB* and *PhCRR*, extra extended region for half wavelength are counted in their device footprints, as shown in Figs. A-1(b) and (c).

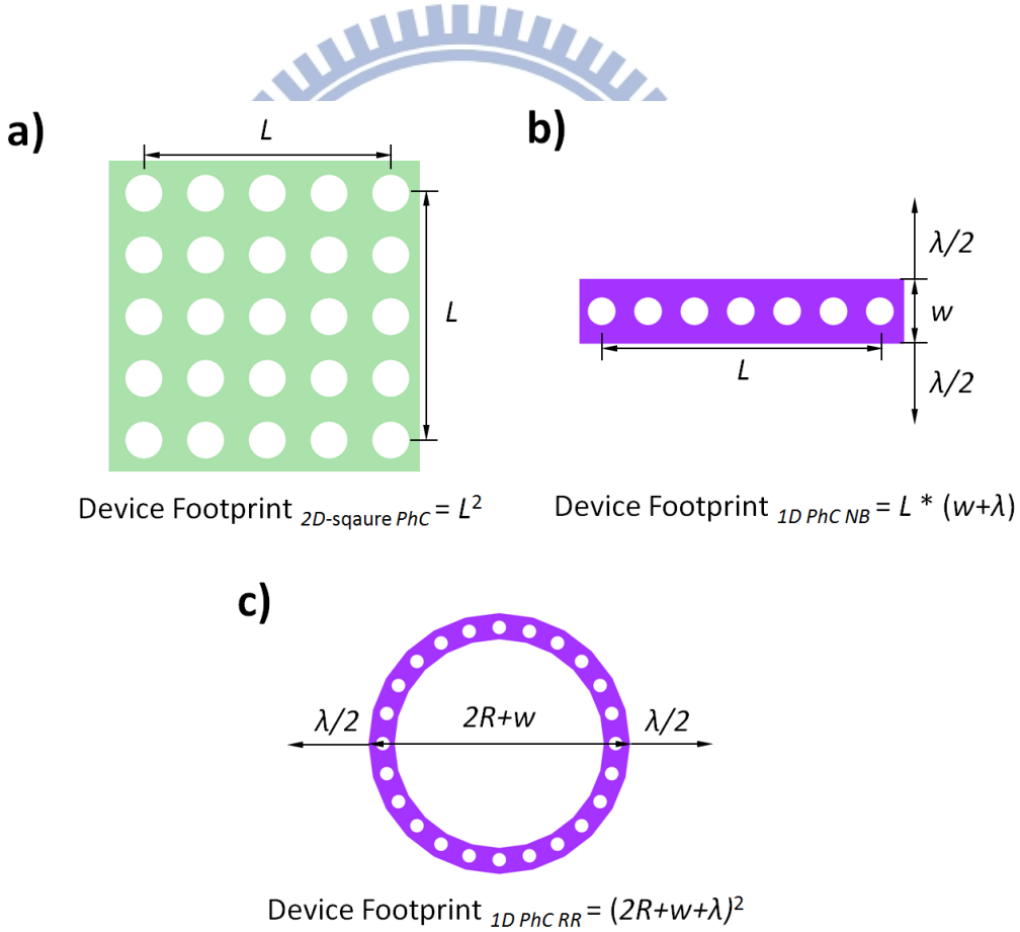


Fig. A-1: Definitions of device footprints of (a) *2D* square-*PhCs*, (b) *1D PhC NB*, and (c) *1D PhCRR*.

# References


[1] E. Yablonovitch, "Inhibited Spontaneous Emission in Solid-State Physics and Electronics," *Phys. Rev. Lett.*, **58**, pp. 2059-2062 (1987).

[2] S. John, "Strong Localization of Photons in Certain Disordered Dielectric Superlattices," *Phys. Rev. Lett.*, **58**, pp. 2486-2489 (1987).

[3] A. Shinya, S. Mitsugi, E. Kuramochi, and M. Notomi, "Ultrasmall multi-channel resonant-tunneling filter using mode gap of width-tuned photonic-crystal waveguide," *Opt. Express*, **13**, pp. 4202-4209 (2005).

[4] H. Takano, B. S. Song, T. Asano and S. Noda, "Highly efficient multi-channel drop filter in a two-dimensional hetero photonic crystal," *Opt. Express*, **14**, pp. 3491-3496 (2006).

[5] T. Tanabe, M. Notomi, S. Mitsugi, A. Shinya, and E. Kuramochi, "Fast bistable all-optical switch memory on a silicon photonic crystal on-chip," *Opt. Lett.*, **30**, pp. 2575-2577 (2005).

[6] Y. Liu, F. Qin, Z. M. Meng, F. Zhou, Q. H. Mao, and Z. Y. Li, "All-optical logical gates based on two-dimensional low-refractive-index nonlinear photonic crystal slabs," *Opt. Express*, **19**, pp. 1945-1953 (2011).

[7] M. Lonĉar, T. Yoshie, A. Scherer, P. Gogna, and Y. Qiu, "Low-threshold photonic crystal laser," *Appl. Phys. Lett.*, **81**, pp. 2680-2682 (2002).

[8] S. H. Kwon, H. Y. Ryu, G. H. Kim, and Y. H. Lee, "Photonic bandedge lasers in two-dimensional square-lattice photonic crystal slab," *Appl. Phys. Lett.*, **83**, pp. 3870-3872 (2003).

[9] H. G. Park, S. H. Kim, S. H. Kwon, Y. G. Ju, J. K. Yang, J. H. Baek, S. B. Kim, and Y. H. Lee, "Electrically Driven Single-Cell Photonic Crystal Laser," *Science*, **305**, pp. 1444-1447 (2004).

[10] O. Painter, R. K. Lee, A. Scherer, A. Yariv, J. D. O'Brien, P. D. Dapukus, and I. Kim, "Two-Dimensional Photonic Band-Gap Defect Mode Laser," *Science*, **284**, pp. 1819-1821 (1999).

[11] J. P. Dowling, M. Scalora, M. J. Bloemer, and C. M. Bowden, "The photonic band edge laser: A new approach to gain enhancement," *J. Appl. Phys.*, **75**, pp. 1896-1899 (1994).

[12] C.O. Cho, J. Jeong, J. Lee, H. Jeon, I. Kim, D. H. Jang, Y. S. Park, and J. C. Woo, "Photonic crystal band edge laser array with a holographically generated square-lattice pattern," *Appl. Phys. Lett.* **87**, 161102 (2005).

[13] V. Reboud, P. Levera, N. Kehagias, M. Zelsmann, C. Schuster, F. Reuther, G. Gruetzner, G. Redmond, and C. M. S. Torres, "Two-dimensional polymer photonic crystal band-edge lasers fabricated by nanoimprint lithography," *Appl. Phys. Lett.* **91**, 151101 (2007).

[14] S.Ahn, H. Kim, H. Jeon, J. R. Oh, Y. R. Do, and H. J. Kim, "Two-Dimensional Hexagonal Lattice Photonic Crystal Band-Edge Laser Patterned by Nanosphere Lithography," *Appl. Phys. Express,* **5**, 042102 (2012).

[15] K. Nozaki, S. Kita, and T. Baba, "Room temperature continuous wave operation and controlled spontaneous emission in ultrasmall photonic crystal nanolaser," *Opt. Express*, **15**, pp. 7506-7514 (2007).

[16] S. Matsuo, A. Shinya, T. Kakitsuka, K. Nozaki, T. Segawa, T. Sato, Y. Kawaguchi, and M. Notomi, "High-speed ultracompact buried heterostructure photonic-crystal laser with 13fJ of energy consumed per bit transmitted," *Nat. Photonics* **4**, pp. 648-654 (2010).

[17] T. W. Lu, S. P. Lu, L. H. Chiu, and P. T. Lee, "Square lattice photonic crystal surface mode lasers," *Opt. Express,* **18**, pp. 2646-26468 (2010).

[18] S. Matsuo, K. Takeda, T. Sato, M. Notomi, A. Shinya, K. Nozaki, H. Taniyama, K. Hasebe, and T. Kakitsuka, "Room-temperature continuous-wave operation of lateral current injection wavelength-scale embedded active-region photonic-crystal laser," *Opt. Express*, **20**, pp. 3773-3780 (2012).

[19] E. Kuramochi, H. Taniyama, T. Tanabe, A. Shinya, and M. Notomi, "Ultrahigh-Q two-dimensional photonic crystal slab nanocavities in very thin barriers," *Appl. Phys. Lett.* **93**, 111112 (2008).

[20] Y. Takahashi, Y. Tanaka, H. Hagino, T. Sugiya, Y. Sato, T. Asano, and S. Noda, "Design and demonstration of high-*Q* photonic heterostructure nanocavities suitable for integration," *Opt. Express* **17**, pp. 18093-18102 (2009).

[21] J. S. Foresi, P. R. Villeneuve, J. Ferrera, E. R. Thoen, G. Steinmeyer, S. Fan, J. D. Joannopoulos, L. C. Kimerling, H. I. Smith, and E. P. Ippen, "Photonic-bandgap microcavities in optical waveguides," *Nature* **390**, pp. 143-145 (1997).

[22] M. Notomi, E. Kuramochi, and H. Taniyama, "Ultrahigh-*Q* Nanocavity with *1D* Photonic Gap," *Opt. Express,* **15**, pp. 11095-11102 (2008).

[23] B. H. Ahn, J. H. Kang, M. K. Kim, J. H. Song, B. Min, K. S. Kim, and Y. H. Lee, "One-dimensional parabolic-beam photonic crystal laser," *Opt. Express,* **18**, pp. 5654-5660 (2010).

[24] Y. Gong, B. Ellis, G. Shambat, T. Sarmiento, J. S. Harris, and J. Vuĉković, "Nanobeam photonic crystal cavity quantum dot laser," *Opt. Express* **18**, pp. 8781-8789 (2010).

[25] Y. Zhang, M. Khan, Y. Huang, J. Ryou, P. Deotare, R. Dupuis and M. Lončar, "Photonic crystal nanobeam lasers," *Appl. Phys. Lett.*, **97**, 051104 (2010).

[26] S. Kim, B. H. Ahn, J. Y. Kim, K. Y. Jeong, K. S. Kim, and Y. H. Lee, "Nanobeam photonic bandedge laser," *Opt. Express* **19**, pp. 24055-24060 (2011).

[27] B. Wang, M. A. Dündar, R. Nötzel, F. Karouta, S. He, and Rob W. van der Heijden, "Photonic crystal slot nanobeam slow light waveguides for refractive index sensing," *Appl. Phys. Lett.* **97**, 151105 (2010).

[28] S. Lin, J. Hu, L. Kimerling, and K. Crozier, "Designed of nanoslotted photonic crystal waveguide cavities for single nanoparticle trapping and detection," *Opt. Lett.* **34**, pp. 3451-3453 (2009).

[29] M. Eichenfield, R. Camacho, J. Chan, K. J. Vahala, and O. Painter, "A pictogram- and nanometre- scale photonic-crystal optomechanical cavity," *Nature* **459**, pp. 550-556 (2009).

[30] G. Shambat, B. Ellis, J. Petykiewicz, M. A. Mayer, T. Sarmiento, J. Harris, E. E. Haller, and J. Vuĉković, "Nanobeam photonic crystal cavity light-emitting diodes," *Appl. Phys. Lett.* **99**, 071105 (2011).

[31] J. J. Wierer, D. A. Steigerwald, M. R. Krames, J. J. O'Shea, M. J. Ludowise, G. Christenson, Y. C. Shen, C. Lowery, P. S. Martin, S. Subramanya, W. Gotz, N. F. Gardner, R. S. Kern, and S. A. Stockman, "High power AlGaInN flip-chip light-emitting diodes," *Appl. Phys. Lett.,* **78**, pp. 3379-3381 (2001).

[32] D. Fehly, A. Schlachetzki, A. S. Bakin, A. Guttzeit, and H. H. Wehmann, "Monolithic InGaAsP Optoelectronic Devices With Silicon Electronics," *IEEE J. Quantum Electron.*, **37**, pp. 1246-1252 (2001).

[33] S. N. Farrens, J. R. Dekker, K. Smith, and B. E. Roberds, "Chemical Free Room Temperature Wafer to Wafer Direct Bonding," *J. Electrochem. Soc.* **142**, pp. 3949-3955 (1995).

[34] G. Vecchi, F. Raineri, I. Sagnes, A. Yacomotti, P. Monnier, T. J. Karle, Y. H. Lee, R. Braive, L. L. Gratiet, S. Guilet, G. Beaudoin, A. Talneau, S. Bouchoule, A. Levenson, and R. Raj, "Continuous-wave operation of photonic band-edge laser near 1.55 m on silicon wafer," *Opt. Express* **15**, pp. 7551-7556 (2007).

[35] H. C. Lin, K. L. Chang, G. W. Pickrell, K. C. Hsieh, and K. Y. Cheng, "Low temperature wafer bonding by spin-on-glass," *J. Vac. Sci. Technol. B* **20**, pp. 752-754 (2002).

[36] G. Roelkens, D. V. Thourhout, and R. Baets, "Ultra-thin benzocyclobutene bonding of III-V dies onto SOI substrate," *Electron. Lett.* **41**, pp. 561-562 (2005).

[37] L. Liu, G. Roelkens, J. V. Campenhout, J. Brouckaert, D. V. Thourhout, and R. Baets, "III-V/Silicon-on-Insulator Nanophotonic Cavities for Optical Network-on-Chip," *J. Nanosci. Nanotechnol.*, **10**, pp. 1461-1472 (2010).

[38] T. J. Karle, Y. Halioua, F. Raineri, P. Monnier, R. Braive, L. L. Gratiet, G. Beaudoin, I. Sangnes, G. Roelkens, F. V. Laere, D. V. Thourhout, and R. Raj, "Heterogeneous integration and precise alignment of InP-based photonic crystal lasers to CMOS fabricated silicon-on-insulator wire waveguides," *J. Appl. Phys.* **107**, 063103 (2010).

[39] Y. Halioua, A. Bazin, P. Monnier, T. J. Karle, I. Sagnes, G. Roelkens, D. V. Thourhout, F. Raineri and R. Raj, "III-V photonic crystal wire cavity laser on silicon wafer," *J. Opt. Soc. Am. B*, **27**, pp. 2146-2150 (2010).

[40] S. H. Kim, H. Y. Ryu, H. G. Park, G. H. Kim, Y. S. Choi, Y. H. Lee, and J. S. Kim, "Two-dimensional photonic crystal hexagonal waveguide ring laser," *Appl. Phys. Lett.* **81**, pp. 2499-2501 (2002).

[41] A. R. Alija, L. J. Martinez, P. A. Postigo, C. Seassal, and P. Viktorovitch, "Coupled-cavity two-dimensional photonic crystal waveguide ring laser," *Appl. Phys. Lett.*, **89**, 101102 (2006).

[42] Z. Qiang, W. Zhou, and R. A. Soref, "Optical add-drop filters based on photonic crystal ring resonators," *Opt. Express* **15**, pp. 1823-1831 (2007).

[43] P. Andalib and N. Granpayeh, "All-optical ultracompact photonic crystal AND gate based on nonlinear ring resonators," *J. Opt. Soc. Am. B*, **26**, pp. 10-16 (2009).

[44] J. Sugisaka, N. Yamamoto, M. Okano, K. Komori, and M. Itoh, "Demonstration of the wide control range Q factor of ring cavity with ultrashort directional coupler and curved photonic-crystal ring waveguide," *J. Opt. Soc. Am. B* **6**, pp. 1521-1527 (2012).

[45] K. Nozaki, A. Nakagawa, D. Sano, and T. Baba, "Ultralow Threshold and Single-Mode Lasing in Microgear Lasers and Its Fusion With Quasi-Periodic Photonic Crystals," *IEEE. J. Sel. Top. Quantum Electron.* **9**, pp. 1355-1360 (2003).

[46] Y. Zhang, C. Hamsen, J. T. Choy, Y. Huang, J. H. Ryou, R. D. Dupuis, and M. Lončar, "Photonic crystal disk lasers," *Opt. Lett.* **36**, pp. 2704-2706 (2011).

[47] J. Jin, "The Finite Element Method in Electromagnetics," *2nd Ed, Wiley, New York,* (2002).

[48] W. Y. Chiu, T. W. Huang, Y. H. Wu, Y. J. Chan, C. H. Hou, H. T. Chien, and C. C. Chen, "A photonic crystal ring resonator formed by SOI nano-rods," *Opt. Express* **15**, pp. 15500-15506 (2007).

# Vita

**Wei-Chih Tsai** was born on 25, September, 1987 in Taoyuan, Taiwan. He received the B.S. degree from the Department of Physics, National Central University, Zhongli, Taiwan, in 2010 and the M.S. degree from the Display Institute, National Chiao Tung University, Hsinchu, Taiwan, in 2012. His research was focused on integration of photonic crystal lasers with small footprints on $SiO_2$ substrate.

## Publications:

[1] **Wei-Chih Tsai**, Li-Hsun Chiu, Che-Yao Wu, Tsan-Wen Lu, and Po-Tsung Lee, "One-Dimensional Photonic Crystal Nanocavity Laser and its Capability in Optical Sensing," A-TH-I 2-6, *IPC'11*, Tainan, Taiwan (2011).